Internship (AE5050)

—

Report

Marie Chambe – 4738276

October 7, 2018

ANALYSIS OF PLUTO THOLINS AS POTENTIAL ANALOGUES FOR THE DARK MATERIAL COVERING LOW REFLECTANCE TERRAINS OF PLUTO

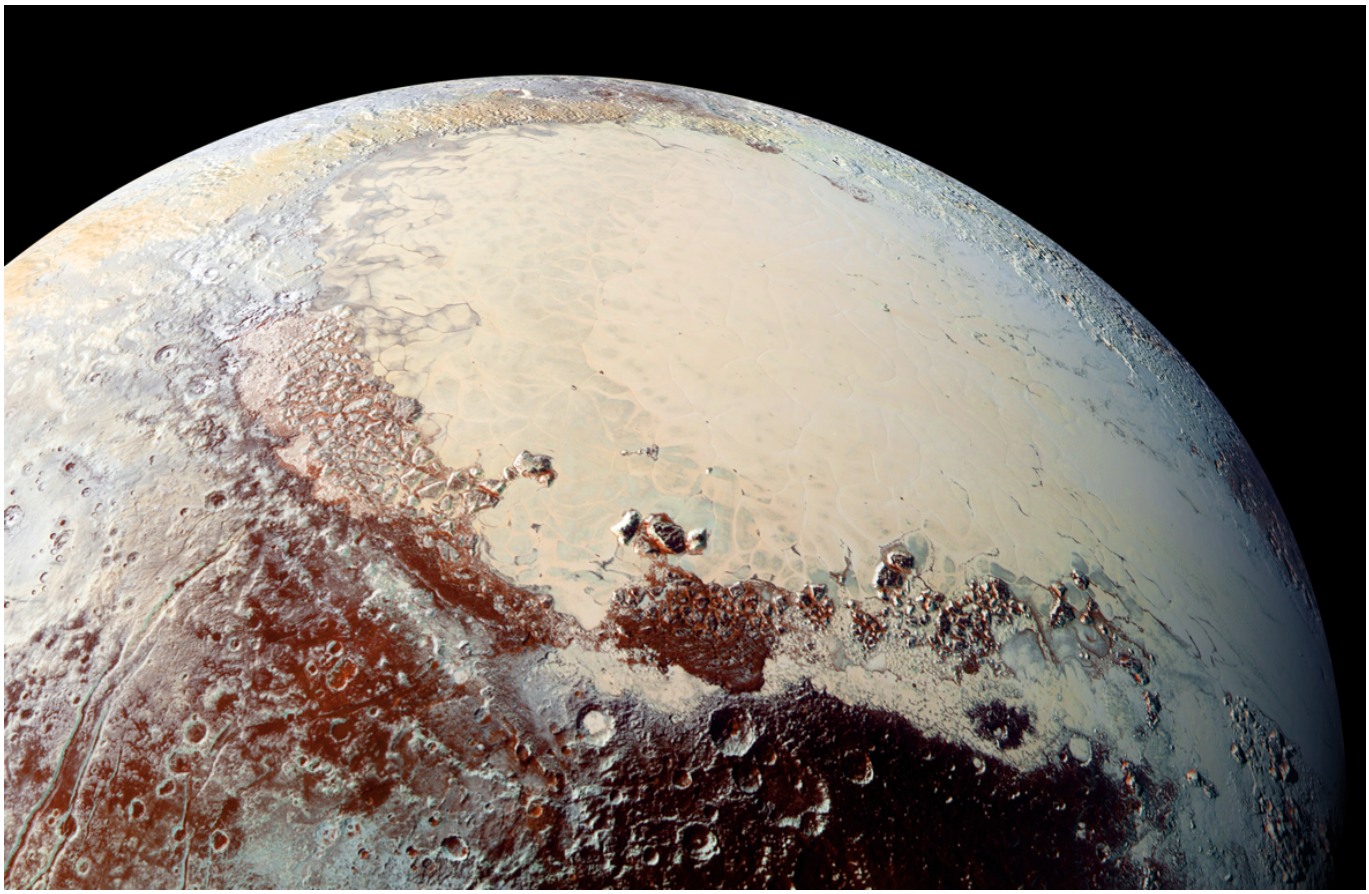

Credit: NASA/JHUAPL/SwRI

Internship coordinator: **Eric Quirico**

Internship performed at IPAG (French acronym for Grenoble Planetology and Astrophysics Institute)

Preface

This internship took place in IPAG (French acronym for Grenoble Planetary and Astrophysics Institute), in Grenoble, France from May to September, 2018 (included). The choice of the planetary sciences field for my internship was motivated by the will to confirm/infirm my future career choices. As I was hesitating at the very beginning of my master studies between astrodynamics and planetary sciences, I have chosen to do my master thesis in astrodynamics and to apply for an internship in a planetary-related research institute. The choice of doing my internship in an research institute instead of an industrial company was also done in order to confirm the plan I have to orient myself to a research career.

I would like to generally thank all the members of the Planeto team who have welcomed me during this internship. Their welcome and availability at any time has turned my internship into a very enjoyable experience. It has been especially very nice of them to always be available for questions and this has been of a great help to get familiar with the planetary sciences framework.

Many thanks to my internship coordinator Eric for guiding me through the whole project I have been working on. I would like to first thank him for welcoming me for this internship, despite the poor background I had in planetary sciences. The help he provided me with at the very beginning of my stay in IPAG to get familiar with the subject I was supposed to work on has really allowed me to start the project rapidly and to catch up with the knowledge I was missing. His encouragements all along the internship have been really helpful to gain more self-confidence and have therefore encouraged me to go deeper in the project. Regular meetings together have provided a clear structure to the work I performed during this internship and have been very helpful to draw intermediate conclusions (which was very necessary in such a wide project). I have appreciated the working autonomy he has given me, while always staying aware of the progress of my work. In addition to that, he has always been available for questions or hints concerning both the technical aspects of the project but also the whole direction to be given to our research work. Finally, many thanks for taking me to Berlin for the European Planetary Sciences Congress. This has been an amazing experience I will certainly remember.

Thanks to Bernard too for the presentation of New Horizons data and the hints he has provided me with to post-process them. The regular meeting points we had when I was working on these data have been very insightful. Generally, his extremely good knowledge of New Horizons data and his availability during the whole duration of my internship have been of great help.

I am very thankful to Sandra and Olivier B. for their help in the use of the laboratory spectro-goniometers. Their explanations have been extremely useful. Many thanks to Sandra in particular for allowing me experimental time with her goniometer SHADOWS, for always being available to answer my questions about the way to use it and for providing me with insightful explanations about the way the instrument was developed.

I would like to thank Nathalie and Thomas from the LATMOS (French acronym for Atmospheres, Mediums and Spatial Observations Laboratory) for providing us with the samples we have been working on and also for the few meetings we had to summarise the progress of our work. These meetings were very nice opportunities to look back at the work we have done and to discuss our main concluding points. Their feedbacks on our conclusions and their remarks about the way the work should be pursued were extremely helpful.

Thanks to Olivier P. for making me take part in his very interesting sublimation experiments and for providing me with detailed explanations about the sublimation process and its possible consequences. This was a very interesting laboratory task I have been glad to discover.

Finally, many thanks to Will and Jason from the New Horizons team for the interesting discussions we had about the reflectance model. It has been of significant help to validate our respective models and it was very impacting to discuss the different ways we were using the same model. I would really like to thank them for this since these discussions have been quite time-consuming and they have put a lot of efforts in it.

Contents

List of Figures

List of Tables

1 List of symbols and abbreviations

SYMBOL OR ABBREVIATION	MEANING
α	Absorption coefficient
b	First parameter of the Henyey-Greenstein function
B_0	Opposition effect coefficient
B_{CB}	Coherent-Backscattering Opposition Effect term
B_{SH}	Shadow-Hiding Opposition Effect term
c	Second parameter of the Henyey-Greenstein function
D	Particles mean diameter
$\langle D \rangle$	Path length of rays through mean particle
e	Emergence angle
ϵ	Dielectric constant
ϵ_{eff}	Dielectric constant of an effective medium
f	Fraction of the total mixture covered by a given particular material in a spatial mixture
g	Phase angle
h	Angular width of the opposition effect
H	Multiple-scattering function
i	Incidence angle
I/F	Radiance factor
k	Imaginary part of the refractive index
k_{eff}	Imaginary part of the refractive index of an effective medium
K	Porosity factor
λ	Wavelength
m	Refractive index
m_{eff}	Refractive index of an effective medium
μ	Cosinus of the incidence angle
μ_0	Cosinus of the emergence angle
μ_e	Cosinus of the effective incidence angle (incidence angle of a equivalent smooth surface, depending on the roughness of the actual surface)
μ_{0e}	Cosinus of the effective emergence angle (emergence angle of a equivalent smooth surface, depending on the roughness of the actual surface)
n	Real part of the refractive index
n_{eff}	Real part of the refractive index of an effective medium
P	Phase function
Ψ	Azimuth angle
Q_e	Extinction efficiency
Q_s	Scattering efficiency
r	Bidirectional reflectance
RADF	Radiance factor (other notation in addition to I/F)
REFF	Reflectance factor
ρ	Solid density
S	Shadowing function
$S(0)$	Specular component of the particle scattering function
SSA	Abbreviation for Single Scattering Albedo
T	Temperature
$\bar{\theta}$	Macroscopic roughness parameter
w	Single scattering albedo

2 Problem statement and methodology

Pluto's flyby performed by the New Horizons spacecraft in July, 2015 has provided additional insights about the composition of its surface. The presence of some ices such as N_2, CH_4 and CO ices was already identified (mostly by Earth-based observations) by the time New Horizons did its flyby. H_2O-ice as well as C_2H_6-ice were also suspected to be present on the surface of Pluto even if they were not unambiguously proved to be so at that time. Visible and near-infrared spectra collected by New Horizons have confirmed the presence of solid N_2, CH_4, CO and also of H_2O-ice on Pluto. Moreover, New Horizons data have brought more understanding about the way those ices are mixed together and distributed. Still the surfaces of some of Pluto's regions are not yet well understood. Some regions indeed show relatively low reflectance levels, which advocates for the presence of another, non-icy material. These regions correspond to the dark-red regions located around the equatorial belt of Pluto. The dark material covering these regions has not yet been definitively identified but complex macromolecular organic materials similar to those forming Titan's haze are presented as the best potential analogues as yet. Indeed, the dark-red regions at the surface of Pluto show very low reflectances in the visible and, on the contrary, high reflectances in the near-infrared. So they present a strong red slope which looks like the one showed by Titan's haze particles. Moreover, these complex organic materials on Titan (the so-called **tholins**) arise from the dissociation of N_2 and CH_4 gases dominating Titan's atmosphere. Dissociation of C-H bonds in CH_4 and N-N bonds in N_2 is induced by both UV-photons and charged particles (photolysis and radiolysis respectively). The products of such a dissociation process can then evolve to form complex macroscopic organic particles which compose Titan's haze but also condense and end up covering Titan's surface. Because Pluto's thin atmosphere is dominated by CH_4, N_2 and CO gases, the radiolysis and photolysis processes from which the formation of tholins originates on Titan are plausible to occur on Pluto as well. The composition of Pluto's tholins might differ from that of Titan's tholins but we could still expect the presence of such complex organic compounds which could possibly explain the low reflectance terrains identified on Pluto.

This internship was about investigating to what extend tholins are relevant analogues for the dark material present in the dark regions of Pluto's surface, especially in Cthulhu region which is among the reddest and darkest regions of Pluto (for the sake of clarity, a map of Pluto is provided in Figure 1). To this end, we were provided with some Pluto tholins by the Nathalie Carrasco and Thomas Gautier from LATMOS (French acronym for Atmospheres, Mediums, Spatial observations Laboratory). The tholins have been synthesised in LATMOS from an initial gas mix whose composition is similar to that of the upper atmosphere of Pluto. The experimental part of this internship has consisted in measuring the reflectance of these tholins under various observation and illumination geometries with a spectrogoniometer. After has followed a step of post-processing of the results (spectral information, scattering behaviour) which aimed at better characterising those Pluto tholins. In parallel to these experiments-related tasks, we also have had access to New Horizons spectral data, for comparison purposes with respect to our laboratory measurements. The analysis of these data we performed has brought more insights and guidelines to our experimental work. The analysis of New Horizons data and the comparison between those data and our own measurements have highlighted the need for additional experiments to confirm/infirm some of the hypotheses that had been made. The alternating between measurements on one side and analysis of New Horizons data on the other side has driven the internship, these two steps being conducted with evolved purposes as we moved forward. In addition to these dual tasks, some numerical tools have been developed and used to support the analysis and help the comparison between laboratory measurements and New Horizons data.

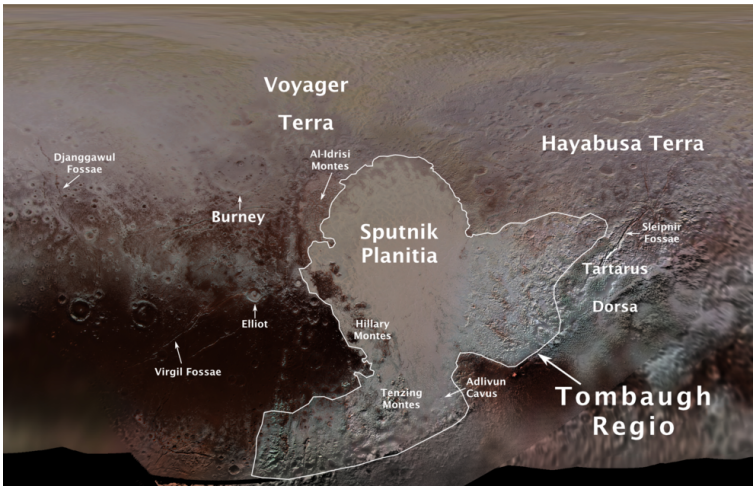

Figure 1: Pluto's map with official name (from NASA official website)
Cthulhu region refers to the region covered with the dark-red material west of Sputnik Planitia.

3 Presentation of the work done and steps that were taken

3.1 Useful definitions and principles to introduce photometry analysis

The flux reflected by a surface depends on the properties of this surface. This is of particular interest as studying the reflected flux can give us access to numerous information about the surface. The geometry under which we are observing the surface and therefore collecting data about its photometry is described in the sketch below (the surface being illuminated under an incident angle i and observed under an emergent angle e).

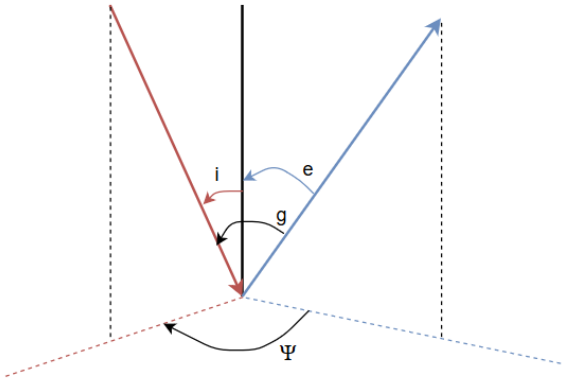

Figure 2: Illumination and observation geometry

The phase angle g is given by the following relation:

$$\cos(g) = \cos(e)\cos(i) + \sin(e)\sin(i)\cos(\Psi) \tag{1}$$

So the phase angle g differs from $|i - e|$ if the emergent and incident planes are not coplanar. It depends on the azimuth angle Ψ as well.

At this point, it is worth introducing some important notions and variables which will be particularly useful to describe the photometric properties of the surfaces we will be dealing with.

- The **radiance** defines the power reflected in a given direction per surface area and per solid angle (expressed in $\mathrm{Wm^{-2}sr^{-1}}$)
- The **irradiance** refers to power reflected in a given direction per unit surface (expressed in $\mathrm{Wm^{-2}}$).
- The **bidirectional reflectance** $\boldsymbol{r}$ is the ratio of the scattered radiance (radiance which emerges along a given direction from a surface illuminated by a collimated irradiance) to the incident irradiance. If we note I the radiance, J the irradiance and μ_0 the cosinus of the incidence angle, then the bidirectional reflectance is expressed as follows:

$$r = \frac{I \cdot \mu_0}{J} \tag{2}$$

- The **reflectance** corresponds to the fraction of the incident flux that is scattered by a given surface.
- The reflectance factor **REFF** (dimensionless) is the ratio between the reflectance of the surface we are considering and that of a perfect lambertian surface. These two surfaces (the actual and the lambertian ones) are supposed to be observed and illumined under the same geometry. The reflectance factor is related to the bidirectional reflectance by:

$$\mathrm{REFF} = \frac{\pi \cdot r}{\mu_0} \text{ where: } \mu_0 = \cos(i) \tag{3}$$

  because the reflectance of a lambertian surface is equal to μ_0/π

- Radiance factor I/F (dimensionless) is the ratio of the bidirectional reflectance of a surface to that of a lambertian surface illuminated under an incidence of 0. The only difference with respect to the reflectance factor **REFF** is that the lambertian surface is not illuminated under the same incidence as the surface we are interested in but is rather illuminated under i = 0deg. As a result, the radiance factor is obtained by:

$$\mathrm{I/F} = \pi \cdot r \tag{4}$$

  because π corresponds to the reflectance of a lambertian surface illumated under an incidence of 0 deg. The radiance factor is sometimes referred as **RADF**, as it is the case in Hapke (1993).

- The **Single Scattering Albedo (SSA)** is the ratio of the scattered power to the total incident power. It is therefore an indicator of the scattering efficiency of a surface. Indeed, it can also be described as the ratio of the scattering efficiency to the total extinction efficiency (which includes both the scattering and absorption effects). If we note Q_S and Q_E the scattering and extinction efficiencies respectively, the single scattering albedo is given by:

$$w = Q_S/Q_E \tag{5}$$

- The **optical constants n and k** form the real and imaginary parts of the refractive index respectively. k carries the information about the absorption features of the concerned compound. Both of them are involved in the calculation of the single scattering albedo (see Equation 15).

To model the reflectance of a surface, several alternatives exist. Hapke's model is among the most used models since it is quite complete and it takes a lot of phenomena into account such as:

- **Porosity effects** since the reflectance of a surface depends on the porosity of the material(s)
- **Multiple scattering:** the fact that we are dealing with either single or multiple scattering depends on the absorption level. Multiple scattering occurs if the material is transparent enough not to absorb the light too efficiently (can be the case for light materials like ices or bright minerals). On the contrary, dark materials absorb the light in a more efficient way. In this case, it is possible to assume the light will encounter only one particle and will be "directly" absorbed. In the rest of our work, and because we will be dealing with very bright materials in the near-infrared, we will keep considering the multiple scattering (our materials not being dark enough to assume single scattering is occuring).
- **Opposition effect:** it describes the brightness growth observed at very small phase angles (close to 0 deg). This phenomenon actually follows from two combined effects: the so-called *Shadow-Hiding Opposition Effect* (SHOE) and *Coherent Backscattering Opposition Effect* (CBOE). The SHOE contribution to the total opposition effect corresponds to the following phenomenon: each particle is partially hidden by the shadows cast by other particles. However, when the phase angle becomes small enough, this is not true any more since the particles do not cast shadows on other ones in this particular case. This partly explains why we observe an increasing of the reflectance when the phase angle gets close to 0deg. Concerning the CBOE, it is due to the positive interferences which occur between two waves emerging from the medium after having gone through it by the same multiply scattered path but in opposite directions. If the two waves reach the interface with the same incidence and if the phase angle is 0 deg, then the two emerging waves will be phased when leaving the medium and constructive interferences will occur. This leads to the appearance of a brightness peak around phase angles equal to 0 deg.
- **Macroscopic roughness:** indeed, the surface roughness has an impact on its reflectance because it will cast shadows on some particles and can therefore reduce the reflectance. Of course, the shadowing does not only depend on the surface roughness but is also dependent on the observation and illumination geometry,

In the Hapke model, the reflectance is given by the following expression:

$$r(i,e,g) = K\frac{\omega}{4\pi}\frac{\mu_{0e}}{\mu_{0e}+\mu_e}\left[P(g,\lambda)B_{SH}(g) + H(\mu_{0e}/K)H(\mu_e/K) - 1\right]B_{CB}(g)S(i,e,g,\bar{\theta}) \tag{6}$$

where:

- $\mu_{0e} = \cos(i_e)$, i_e being the effective incidence angle which means it is the incidence angle that would correspond to an effective smooth surface (this angle depends on the roughness of the actual surface)
- $\mu_e = \cos(e_e)$, e_e refers to the effective emergence angle (defined in a similar way as the effective emergence angle above)
- Single scattering albedo w
- Porosity parameter K
- Shadowing function $S(i,e,g)$
- $P(g,\lambda)$: phase function
- $B_{SH}(g)$: function modelling the *Shadow Hiding Opposition Effect*
- $B_{CB}(g)$: function modelling the *Coherent Backscattering Opposition Effect*
- $H(\mu_0/K)H(\mu/K)$ represents the multiple scattering and the introduction of the porosity parameter in the model

The different functions involved in the definition of the reflectance will be briefly discussed below. However, for the sake of brevity and because extensive discussions about the numerical details of the model do not bring any additional insight here, the detailed formulae are only provided in appendices (see Appendix 14.1).

1. **Single Scattering Albedo**

   As already stated before, the SSA (Single Scattering Albedo) refers to the ratio between the power scattered to the total power extinct (which corresponds to the sum of the power scattered and the power absorbed) for a single particle. The Single Scattering Albedo depends on the optical constants n and k, as well as on the particles mean diameter and the wavelength.

2. **Shadowing function**

   If we want to take the roughness into account, the reflectance is expressed as follows:

   $$r_{rough}(i, e, g) = r_{flat}(i_e, e_e, g) \times S(i, e, g, \bar{\theta}) \tag{7}$$

   where i_e and e_e are the effective incident and emergent angles, respectively and $S(i, e, g)$ is the shadowing function.

   The shadowing function S depends on the geometry (incident, emergent and azimuth angles) but also on the macroscopic roughness parameter $\bar{\theta}$. $\bar{\theta}$ is an angle characterising the roughness state of the surface. It is worth noting that if this parameter is set to 0 deg (meaning that the surface is perfectly smooth), the shadowing function is equal to 1 and has therefore no impact on the reflectance.

3. **Phase function**

   The phase function describes the probability that a photon has to be scattered in a certain direction (it is the function which describes the fact that the scattering is anisotropic and that some directions are preferred compared to others).

Hapke's model has been widely used in the rest of our work to model surfaces reflectance. To this end, it has been programmed in Matlab, based on its complete formulation (see Equation 6). This tool has been of great help at each step of this project. Although the complete Hapke's model has been implemented in Matlab, we have used a simplified version of Hapke's model for the main part of our work. As we have not been dealing with very small phase angles, the opposition effect has been neglected. Moreover, the porosity and macroscopic roughness effects have been disregarded as well because we have absolutely no information to estimate the associated parameters. As a consequence, taking these effects into account would have led to the addition of too many free parameters. Regarding porosity, despite the fact we are neglecting it here, we should still keep in mind that it can induce significant effects (Poch et al., 2016). These simplifying assumptions have reduced Hapke's formulation to a much more condensed form and have also reduced the number of parameters the reflectance is depending on. The simplified formulation is the following one:

$$r(i, e, g) = \frac{\omega}{4\pi} \frac{\mu_0}{\mu_0 + \mu} \left[P(g, \lambda) + H(\mu_0)H(\mu) - 1\right] \tag{8}$$

3.2 Analysis of New Horizons data

In July 2015, the New Horizons spacecraft has performed a fly-by of Pluto during which the Ralph instrument has retrieved numerous spectral data in the visible and infrared. The point of closest approach of New Horizons with respect to Pluto occurred on July, 14^{th} after about 10 years of space travelling.

The Ralph instrument includes MVIC and LEISA: MVIC is a visible and near-infrared camera and LEISA is an infrared imaging spectrometer. Briefly, MVIC possesses three spectral channels: one referred as the *BLUE* filter, a second one as the *RED* filter and the last one as the *NIR* (near-infrared) filter. The LEISA instrument covers a spectral range going from 1.25 to 2.5 μm. Most of the chemical components suspected to be present at Pluto's surface show absorption features in this spectral range, so that LEISA is able to confirm or infirm their identification.

The calibration of the Ralph instrument was conducted before the launch of the spacecraft. Although some check-in tests have been performed on its way to the outer system, the instruments might still have encountered some calibration issues due to the long 10 years cruise through space. Indeed, some calibration issues have been raised in New Horizons data. During the main part of the internship, discussions were still ongoing to clearly identify these issues and the instrument they are concerning and also to precisely determine the corrections to be applied. The final outcome of these discussions has been that LEISA data must be scaled down by an amount of 15% while MVIC data are underestimated by about 8%. Corrections have been applied accordingly.

The data that have been used had first been post-processed using a Principal Component Analysis in order to filter out the main part of the instrumental noise and to keep the physical part of the signal only (Schmitt et al., 2017). New Horizons data have already been widely analysed but most of the work done was about the repartition of volatile ices (CH_4, N_2...) which have been mapped quite precisely in Schmitt et al. (2017). However, deeper investigations are required in Cthulhu region where clear spectral signatures are missing. A further analysis of the data collected in this dark-red region might help us to conclude about the relevance of tholins as analogues for the non-icy material covering it. We have been provided with the pixels identified as end-members of the red material in Schmitt et al. (2017).

3.2.1 Bands integration

First of all, we have averaged the spectrum over the several pixels identified as end-members of the red material, making three spectral bands emerge: one toward 1.3 μm, a second one about 2-2.1 μm and the last one about 2.3 μm (averaging can indeed help identifying global spectral features that could have barely been detected by looking at the data pixel by pixel because of the noise and local variations). Our aim is now to examine these bands further, especially their spatial repartition across Cthulhu region which could provide us useful insight about their correlation with the presence of the red material.

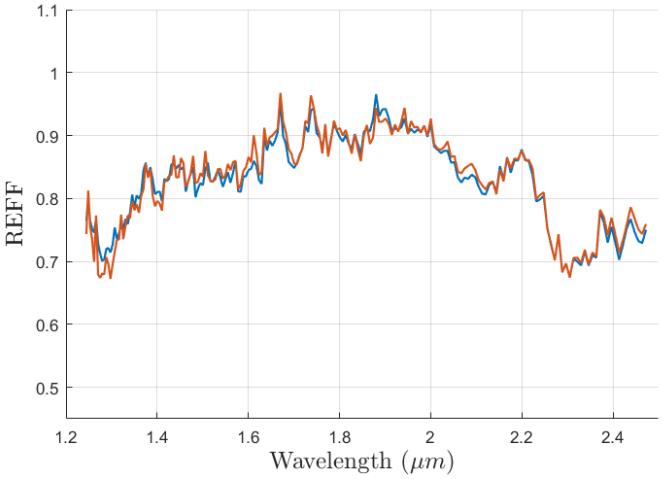

Figure 3: Dark material end-member spectra
The blue curve represents the spectrum which has been averaged over all the pixels identified as end-members of the dark material, while the spectrum of one pixel identified as end-member of the dark material (without any averaging) is plotted in orange.

To this end, we first need to integrate those bands. We use several points for a higher precision. Indeed, instead of integrating the band depth from a starting wavelength λ_1 to an ending wavelength λ_2, we rather first calculate the average of the spectrum values around λ_1 over several wavelengths (and same for λ_2). This aims at reducing errors due to the selection of a single wavelength as the limit of the integration. The averaging of the spectrum values over 3 to 5 values around the original point improves the result of the bands integration (especially since the spectrum might be a bit different or even slightly shifted with respect to the wavelength from one pixel to another one). The integration of each of these three bands was performed using an IDL program and the outcoming data were read with the ENVI software.

The band integral is simply calculated using the following method: we calculate a theoretical slope going from the spectrum value at λ_1 to λ_2 (or between the mean value of the spectrum around λ_1 and λ_2 respectively for the reasons that have just been mentioned above). Then we calculate the band depth, defined as the integral between the spectrum itself and this theoretical slope.

The IDL program determines the band integral for each pixel and this data are read by the ENVI software which can draw maps of the integral band values. This highlights regions where the concerned band is deeper and wider and, on the contrary, regions where this particular band is less pronounced. This has been done for the three bands previously identified (1.3 μm, 2.1 μm and 2.3 μm). The purpose of such maps is to identify some spatial trends which could lead to the assignment of some of these bands to the organic material responsible for the dark reflectance of Cthulhu region.

3.2.2 Results and discussion

The evolution of the band around 2.1 μm seems to be strongly correlated with the presence of water ice across Cthulhu region. Water ice has already been identified in this region (Schmitt et al., 2017), with increasing quantities going from the centre of Cthulhu toward its periphery. If we draw the map of the water ice repartition and of the repartition of the 2.1 μm band, we see a strong superposition (see Figures 4a and 4b). This is logical since these two bands are located very close to each other considering their spectral range. It is therefore hard to decouple them. Plotting different spectra along the mixing line between H_2O-ice and the dark material in Cthulhu region (Figures 5a and 5b), we see that the band toward 2.1 μm in the centre of Cthulhu region becomes wider and deeper when getting closer to water-ice end-member (Virgil Fossa in Cthulhu region). However, this band also shifts (it is more centred around 2.1 μm in the centre of Cthulhu region while it gets closer to 2.0 μm near Virgil Fossa (black and yellow curves in Figure 4b respectively)). We also see that the shape of the band evolves from the centre of Cthulhu region to the H_2O-ice end-member. It is hard to conclude about the assignment of this band: it is not likely to be due to water-ice only for the reasons we have mentioned but there is no clear evidence for this band to be caused by the presence of the dark material covering Cthulhu region. Deeper investigation aiming at deconvolving the two bands (the one around 2.1 μm observed in the centre of Cthulhu region and the 2.0 μm H_2O-ice band) is required here. Our simple analysis has not been able to assign this band precisely. The fact that the band toward 2.1 μm has probably another contribution than H_2O-ice could also explain why the repartition of the 1.5 μm H_2O-ice band is different from the one toward 2.0 μm in Cthulhu region (Schmitt et al., 2017).

Even if we have not been able to conclude about the assignment of this band, we cannot exclude the fact that small amounts of water ice remain in the centre of Cthulhu, partially contributing to the presence of the 2.1 μm, while another material (either the dark material or possibly other ices) with an absorption around 2.1 μm is present and contribute to this band as well.

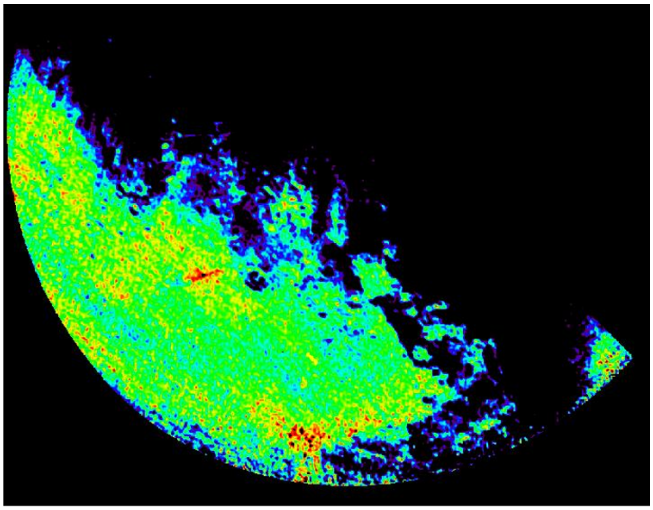

(a) Map of the integrated band toward 2 μm identified in the averaged Cthulhu spectrum

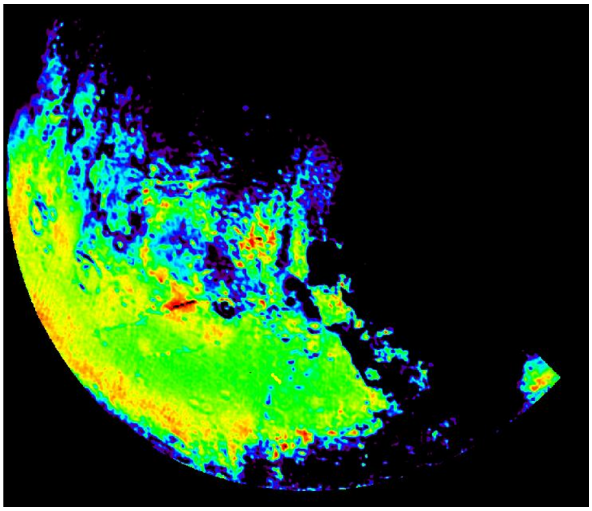

(b) Map of the integrated H_2O band (around 2.0 μm)

Figure 4: Maps of the integrated bands: comparison between the band around 2.0 μm observed in Cthulhu spectra and the H_2O band toward 2.0 μm

The orange-red colours correspond to the highest band integral values while the blue-black colours map the regions where the band integral values are the lowest.

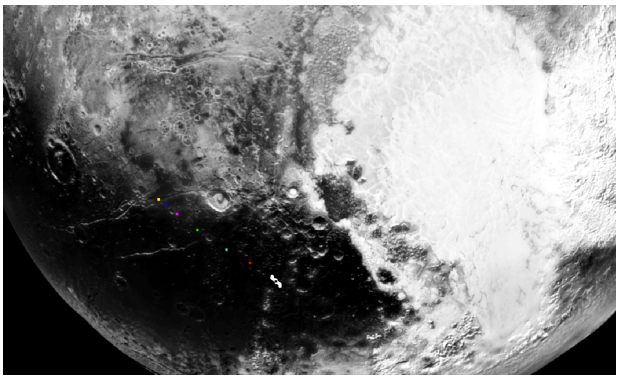

(a) Regions of interest (ROI) along the mixing line between H_2O and the dark material

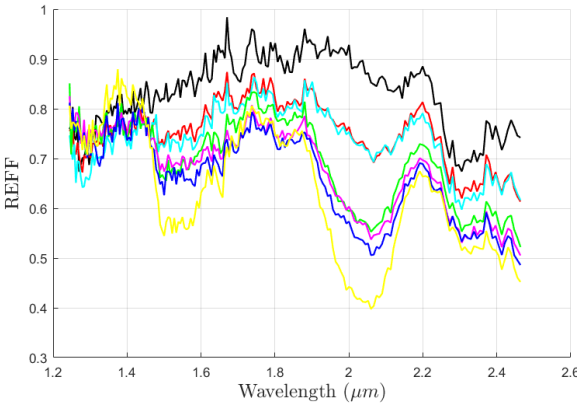

(b) Associated LEISA spectra

Figure 5: Evolution of the LEISA spectra along the mixing line between H_2O-ice and the dark material

The colours of the spectra on the right-hand side figure correspond to that of the ROIs presented on the left-hand side figure. The white patch corresponds to several pixels identified as end-members for the dark material, the black spectrum is picked up in the middle of this "end-member region".

Concerning the band toward 1.3 μm, we do not see any clear spatial distribution which could make us think this band could be linked in any way with the presence of the red material (see Figure 6a). It is also possible that this spectral feature becomes significant because of the averaging but is not as strong while looking at individual spectra.

The last band (around 2.3 μm) is of greater interest. This band is strongly present across the whole Cthulhu region. However it does not seem to significantly evolve spatially (see Figure 6b). Its shape and depth is more or less constant, except when approaching some CH_4-ice rich regions. Indeed, CH_4-ice shows an absorption band around 2.3 μm as well and the band toward 2.3 μm that we observe at the centre of Cthulhu region becomes deeper and wider when going eastward toward the CH_4-rich regions. But this is simply due to the superposition of these two bands around 2.3 μm. To investigate the transition between the region covered with the red material and the CH_4-rich region, we have looked at the spectrum evolution on a mixing line going from the centre of Cthulhu to the CH_4-rich regions located eastwards. Spectra collected along this mixing line have been superposed with each other to visualise the mixing process (see Figures 7a and 7b). At the very first look, the continuity which seems to exist between the 2.3 μm band at the centre of Cthulhu and that in the CH_4-rich region could indicate that the band toward 2.3 μm is due to the presence of some methane ice in which tholins are diluted. Indeed, the transition between the two regions is pretty smooth and the shape of the 2.3 μm band at the centre of Cthulhu is not that different from that in the CH_4-rich region, even if the band grows deeper and wider when getting closer to the CH_4-rich region. The main difference in the band shape is the additional smaller band at 2.2 μm which only appears in the CH_4-rich region.

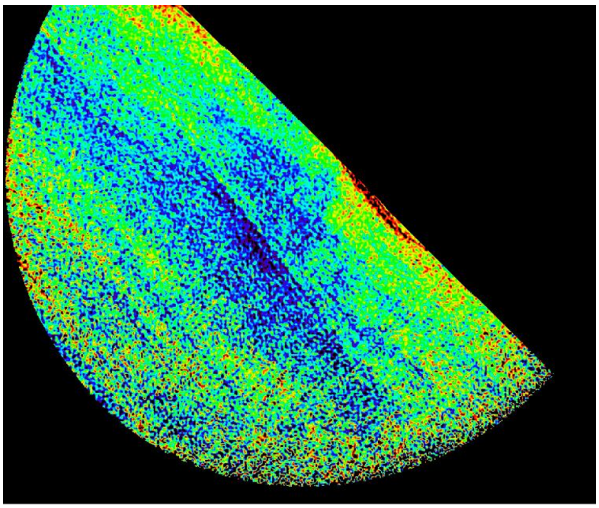

(a) Map of the integrated band toward 1.3 μm identified in the averaged Cthulhu spectrum

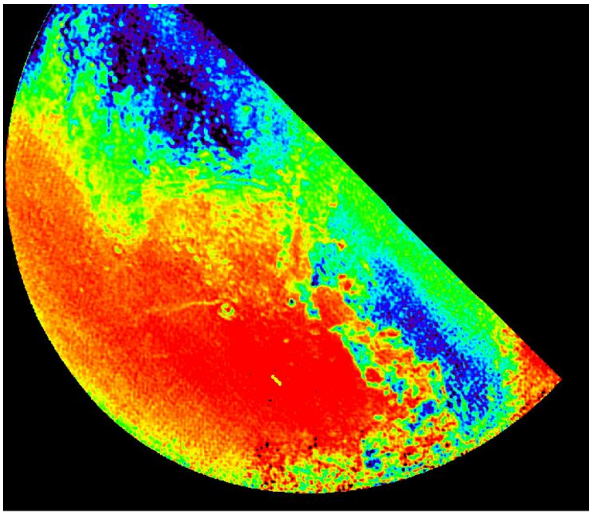

(b) Map of the integrated band toward 2.3 μm identified in the averaged Cthulhu spectrum

Figure 6: Maps of the integrated bands: bands around 1.3 μm and 2.3 μm observed in Cthulhu spectra

The orange-red colours correspond to the highest band integral values while the blue-black colours map the regions where the band integral values are the lowest.

However, the assignment of the 2.3 μm band to CH_4-ice disregards the absence of the other CH_4 bands in Cthulhu's spectra. The fact that these other bands do not appear could be explained if the CH_4-ice were mixed with tholins in such a way that the other bands are strongly attenuated (and therefore undetectable) whereas the bands toward 2.3 μm were still present (plausible since they are very strong bands). To investigate this hypothesis, we have modelled such a mixing between CH_4-ice and tholins, with various ratios between these two components. It aimed at analysing the way CH_4-ice bands are impacted by the progressive addition of tholins and identifying which CH_4 bands totally disappear or rather remain. We have assumed tholins are spatially mixed with CH_4-ice and we have used Hapke's model to calculate the reflectance of such a surface. The results we obtained for various mixing ratios are provided in Figure 8.

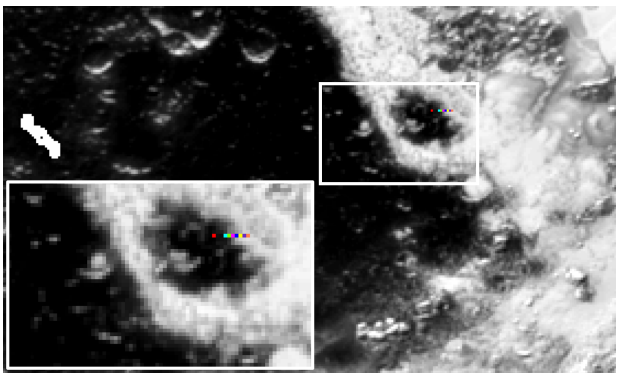

(a) Regions of interest (ROI) along the mixing line between CH_4 and the dark material

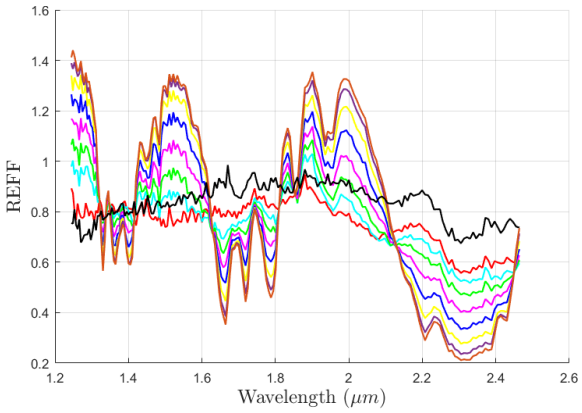

(b) Associated LEISA spectra

Figure 7: Evolution of the LEISA spectra along the mixing line between CH_4-ice and the dark material

The colours of the spectra on the right-hand side figure correspond to that of the ROIs presented on the left-hand side figure. The white patch corresponds to several pixels identified as end-members for the dark material, the black spectrum is picked up in the middle of this "end-member region".

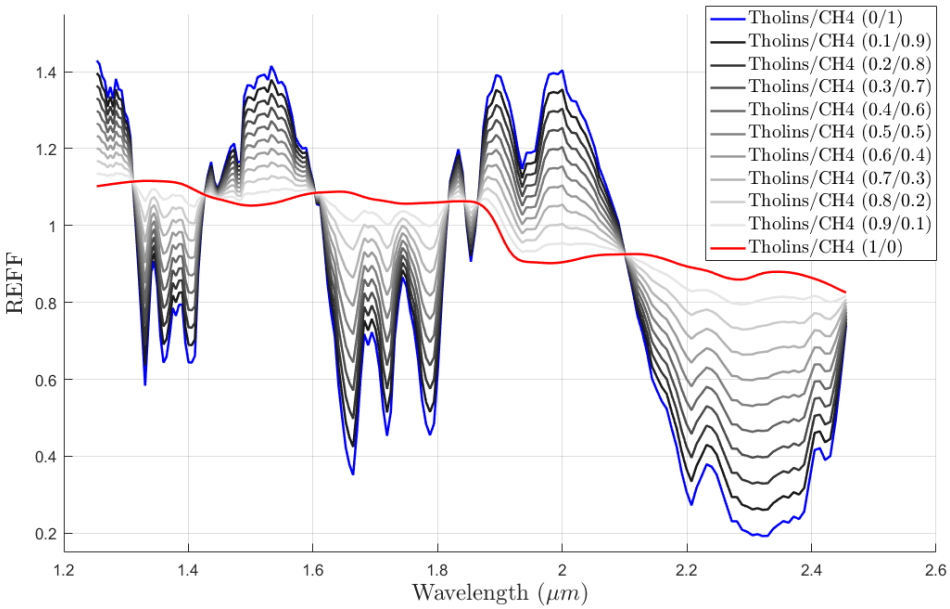

Figure 8: Mixing between CH_4-ice and tholins - based on Hapke's spatial mixing model

It appears that when the bands toward 2.3 μm are still present, the other CH_4-ice bands are present as well. Even with 10% of CH_4-ice only out of 90% of tholins, bands about 1.3-1.4 μm and 1.7-1.8 μm are clearly identifiable and the band about 2.3 μm is not stronger than they are (it is rather the contrary: the wide band about 2.3 μm being less clear than the narrower bands about 1.3-1.4 μm and 1.7-1.8 μm). As a consequence, the 2.3 μm band cannot be entirely assigned to CH_4-ice.

As stated before, the depth and width of the band toward 2.3 μm do not seem to spatially evolve across Cthulhu region. Looking at the mixing line with CH_4-ice, it was not possibly to conclude about the assignment of this band to the organic material. We have indeed found that it cannot be due to the presence of CH_4-ice only because then other bands characteristic of CH_4 would appear. However, the spatial evolution of this band when going toward the CH_4-rich region can be explained by the increasing amount of CH_4, not necessarily by the decreasing amount of tholins as we get further from the centre of Cthulhu.

This is why we have decided to focus on the mixing line between tholins and H_2O-ice. The amount of water ice has been showed to increase when going from the centre of Cthulhu to its periphery (see Figure 4a) whereas the reddest colours of Pluto are located at the centre of Cthulhu. We therefore expect the centre of Cthulhu to contain more tholins diluted in less water ice and the other way around for Cthulhu's periphery. For this particular reason, if the band toward 2.3 μm was due to tholins, we would have expected its shape and depth to evolve along the mixing line with water ice. However, this is not what we have observed. Plotting several spectra corresponding to different pixels distributed along the mixing line between tholins and water ice end-members respectively, we remark that the H_2O bands grow deeper and wider when getting close to the H_2O endmember (as expected) but this is not the case for the band toward 2.3 μm which does not appear to change along this mixing line (see Figure 5b). This band is almost as strong in Virgil Fossa (H_2O endmember) as it is at the centre of Cthulhu.

This observation has led us to the conclusion that this band does not attest for the presence of tholins but is rather due to another component. This also leads to the conclusion that the tholins are somehow transparent spectrally speaking and that their presence is not unveiled by any of the spectral features captured by the LEISA instrument (except a potential contribution to the 2.1 μm band but so far we have not concluded about this band being assigned to the dark material). The presence of the red material would have an impact on the reflectance level only but no clear spectral consequence.

This conclusion is consistent with the findings exposed in Cook et al. (2018), which associate this band to the presence of some hydrocarbon ices, mainly CH_3OH, C_2H_6 and C_3H_8. The paper also clearly states that the model which had been used was based on spectrally transparent tholins.

Concluding points

- The band toward 2.1 μm seems to be only partially explained by the presence of water-ice. Another component is also contributing to this band although we have not yet been able to conclude if this could be the dark material or not.
- The band toward 2.3 μm does not evolve across Cthulhu even when getting closer to the H_2O-rich regions. This band is likely not to be due to CH_4-ice but rather to some other hydrocarbon ices (which is in agreement with the findings exposed in Cook et al. (2018)).

3.3 Tholins preliminary work

3.3.1 Pluto's tholins

To conduct our analysis of tholins as potential analogues for the dark material present on Pluto's surface, we had first been provided with two kinds of tholins synthesised in the LATMOS laboratory (French acronym for Atmospheres, Mediums, Spatial observations Laboratory (Laboratoire AtmosphÃ¨res, Milieux, Observations Spatiales)). There exists many ways to synthesise tholins and thus many different tholins. In LATMOS, tholins synthesis is performed using the PAMPRE experimental set-up. Briefly, a cold plasma discharge is applied to an initial gas mixture at low pressure and room temperature, the gas being mainly composed of N_2, CH_4 and some small quantities of CO. More precisely, a Radio Frequency Capacitively Coupled Plasma (RF CCP) discharge is applied amidst two electrodes between which charged dissociation products levitate and then evolve to form more complex products (the so-called tholins). The two tholins we had been provided with have been synthesised from gas mixes composed of 95% N_2, 5% CH_4, 500 ppm CO and 99% N_2, 1% CH_4, 500 ppm CO respectively. Comparing these initial gas compositions with those of Titan's tholins, the only difference is the incorporation of some small quantities of CO to account for the presence in small amounts of this gas in the upper atmosphere of Pluto (which is not the case for Titan).

3.3.2 Main outcomes of literature study on existing tholins

We do not exactly know the optical constants of these tholins. Indeed, tholins optical constants appear to depend both on the experimental conditions under which tholins have been synthesised (including the initial gas composition, temperature, pressure, the energy source (cold plasma in our case but could has been UV irradiation), the gas flow rate, the duration of the irradiation) and on the way the optical constants are measured. While the conditions of the synthesis have an impact on the chemical composition of the tholins as well as on their grain size and shape, the method used to determine the optical constants also has an influence on the values we get. The same sample but measured with two different techniques can be assigned with different optical constants (Brasse et al., 2015). The high dependency between the optical constants and a huge number of parameters explain why we do not know firmly the optical constants corresponding to our tholins samples.

Among the existing tholins and their estimated optical constants (summarised in Brasse et al. (2015)), those of Khare et al. (1984) are the most widely used. There are two main reasons to explain this: they were the very first tholins optical constants to be published and they are the ones covering the larger wavelength range. However, those synthesised by Mahjoub et al. (2012) and Sciamma-O'Brien et al. (2012) could be more relevant than others since the tholins were synthesised with the PAMPRE experimental set-up too. However, looking at the optical constants that have been deduced from these tholins, we still see some important discrepancies between Mahjoub et al. (2012) tholins and Sciamma-O'Brien et al. (2012) ones (again due to some slight differences in the measurement techniques). Since these tholins have been produced from a gas mixture containing no CO and because there are some uncertainties about the measured optical constants, we will keep in mind that optical constants available in literature are not trustworthy and need to be cautiously considered.

The relevance of the different sets of optical constants found in the literature for our particular samples will be examined further while comparing the reflectance spectra derived from these optical constants to the spectra we will measure in the laboratory. This aims at concluding about whether or not it is consistent to use those optical constants to model the reflectance behaviour of our Pluto's tholins.

3.3.3 Tholins SEM characterisation

To characterize the tholins we have been provided with by the LATMOS laboratory, we have used a SEM (Scanning Electron Microscope). This aimed at estimating the mean tholin size, as well as to investigate which shape distribution the tholins follow. A SEM observation has been performed for each of the two samples we got (below are provided some pictures).

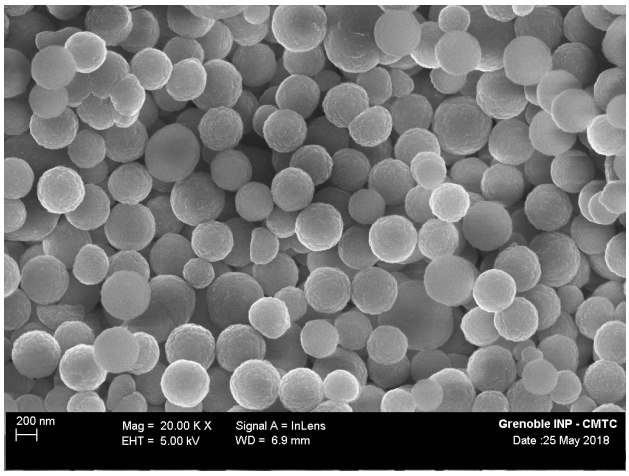

(a) Tholins 95:5 (N_2:CH_4)

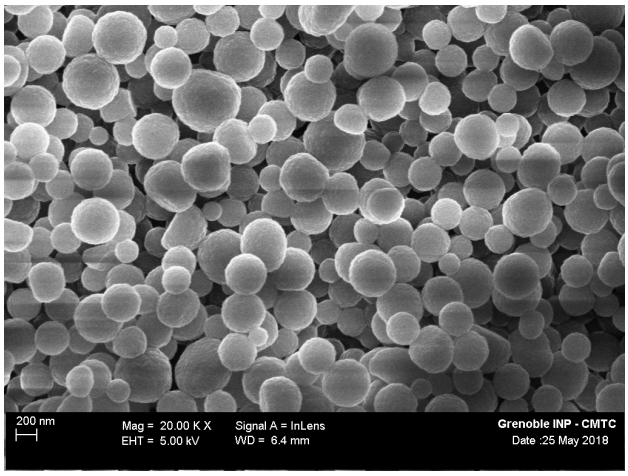

(b) Tholins 99:1 (N_2:CH_4)

Figure 9: SEM observation of the two tholins samples

The tholins are spherical-shaped particles: the shape of 95:5 tholins is slightly more regular than that of 99:1 tholins which do not look like perfect spheres as much as 95:5 tholins do. 95:5 tholins present very regular shape and the tholins seem to have almost identical sizes. The grain size distribution appears to be wider for 99:1 tholins but still the grain sizes do not vary that much. To validate these remarks made only by looking at Figures 9a and 9b, we have estimated the diameters of more than 100 tholins present on each of those pictures respectively using the imageJ software and we have plotted the corresponding grain size distributions.

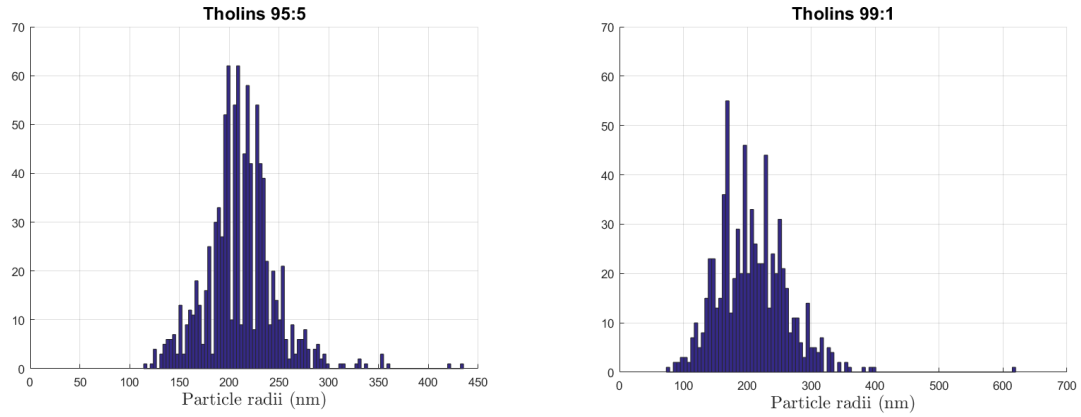

Figure 10: Grain size distribution for both tholins 95:5 and tholins 99:1 (obtained with the imageJ software from the SEM pictures)

We indeed see that the 95:5 tholins present a very narrow size distribution, centred around a mean radius of 210 nm. The size distribution of the 99:1 tholins is, as expected, less narrow. However, the mean radius is about 210 nm as well (207 nm to be exact). The standard deviation for 99:1 tholins is equal to 55 nm, to be compared with 35 nm for 95:5 tholins.

The observation of the tholins samples has provided us with two important information: we now have a good estimation of the mean diameter of our tholins (this is really useful to plug in in Hapke's model) and we know that our tholins are almost perfect spheres.

3.3.4 Analysis of the use of tholins in Grundy et al. (2018) to model Pluto's colours

Tholins have been considered as potential good analogues for the dark material present in some regions of Pluto's surface such as Cthulhu in Grundy et al. (2018). Grundy et al. (2018) proposed to model haze particles as a combination of a matrix made of transparent hydrocarbons ices and of tholins which are acting as coloring agents. In this model, the hydrocarbon ices are assumed to be completely transparent: the real part of the refractive index is therefore equal to a constant value whereas its imaginary part (supposed to carry the absorption information) is set to 0. The ratio ices/tholin was a free parameter of this model. Using Hapke's model combined with Garnett's formulae to calculate the effective properties of the medium, the reflectance of the modelled material has been calculated and has been compared to New Horizons data. Since Grundy et al. (2018) is mostly focused on Pluto's colours, the first match that was attempted was with MVIC data (visible spectral range only), playing around with the parameters of the model (the particle size and the ratio ices/tholins). It has appeared that none of the free parameters combinations has managed to match the MVIC data (the reflectance was too low in the short wavelengths and too high for higher wavelengths). This has led to the addition of internal scatterers in the model as a means to attenuate the colouration of the material. Adding such internal scatterers (whose presence could be justified by the presence of voids in between aggregates which would act as internal scatterers) managed to match MVIC data. However, no way was found to match both MVIC and LEISA data at the same time.

The main issue if we consider that tholins are present but mixed within some hydrocarbon ices is that we expect some absorption features due to the presence of those ices to appear. In Grundy et al. (2018), the hydrocarbon ices were supposed to be featureless but this is certainly not the case in the wavelength range of LEISA. Instead of assuming constant value for n and k set to 0, we have plugged in optical constants of actual hydrocarbon ices in Hapke's model to see if some bands indeed appeared. All the other parameters have been unchanged. Below are provided the reproduction of the results presented in the paper (as a check that our model was consistent with the one used for the paper), as well as the outcome of Hapke's model if we remove the assumption about the ices transparency.

Figure 11a confirms that it is indeed possible to match the MVIC data quite well by introducing internal scatterers (see Appendix 14.1 for the formulae). However, as stated in Grundy et al. (2018), we are not able to match both MVIC and LEISA data. The original LEISA data are presented with the dashed blue curve. W. Grundy has indicated us to have corrected the LEISA data by an amount of 27% to account for the calibration problems (the final estimation of the calibration errors was not made at that time). Our model has led to the same results as those presented in Grundy et al. (2018): mainly the fact we can reproduce MVIC colours only if we add internal scatterers, the tholins spectral slope being too steep otherwise, and that it is apparently not possible to reproduce both MVIC and LEISA data with this haze model.

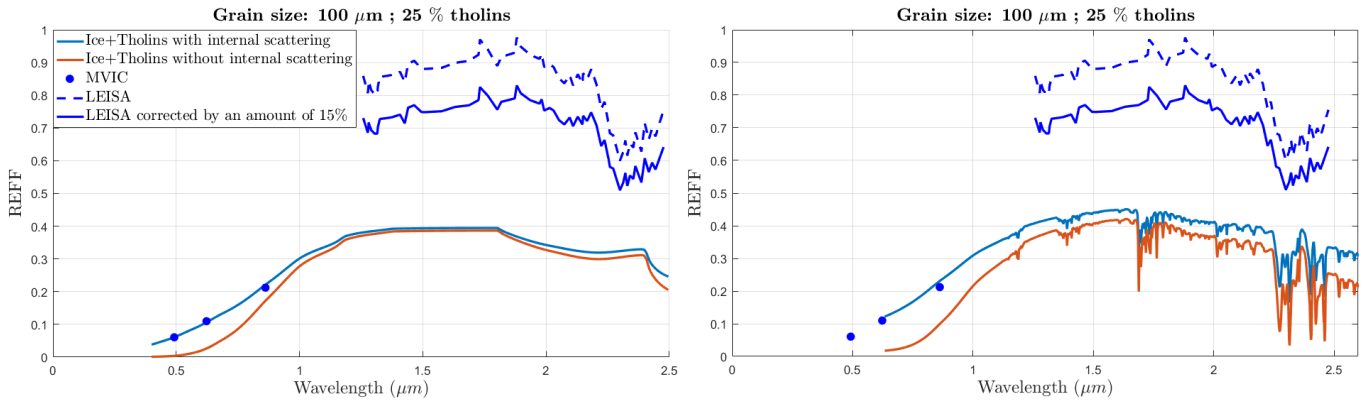

(a) Hydrocarbon ices assumed to be totally transparent

(b) Actual ethane optical constants are plugged in the model

Figure 11: Model of haze particles as a combination of ices surrounding tholins

Figure 11b presents the results we have obtained by running exactly the same model except that we have considered actual optical constants for ethane instead of assuming completely transparent hydrocarbon ices. For comparison purposes, we have kept the other parameters constant. We remark that this time we do not perfectly match the MVIC colours. This slight difference is simply due to the different values we used for the real part of the refractive index n. Using actual ethane optical constants make many bands appear in the near-infrared spectral range, which seems to be rather inconsistent with the LEISA data. The absorption bands toward 2.3 μm could be interesting to explain the presence of the 2.3 μm band in LEISA data but the other ethane absorption features do not appear in New Horizons spectra.

As hydrocarbon ices indeed lead to the appearance of some extra absorption bands which are not present in LEISA spectra, it would require to introduce actual transparent ices (at least transparent in LEISA's spectral range) instead of hydrocarbon ices. N_2 could be a potential candidate since it is transparent in our spectral range of interest. However, the surface temperature is too high in Cthulhu region to allow N_2-rich ices to subsist (too volatile). This raises questions about the validity of the model proposed in Grundy et al. (2018) and again highlights one of the major issues of the determination of Cthulhu's surface composition, being the absence of clear absorption features for both tholins or hydrocarbon ices, except for the 2.3 μm band.

Concluding points

- The grain size distribution of Pluto tholins provided by the LATMOS is very narrow. The mean diameter is about 420 nm for both types of tholins.
- The optical constants available in the literature are extremely different from each other depending on the way tholins have been synthesised but also on the way the optical constants have been determined. They should therefore be considered carefully.
- Our tholins are particularly interesting since they have been formed in conditions close to those under which we can expect tholins to form in Pluto's atmosphere.
- When adding hydrocarbon ices to our reflectance model, use should be made of actual optical constants for ices to avoid missing the appearance of some absorption bands due to the presence of ices.

3.4 Laboratory reflectance measurements

3.4.1 Experimental data and numerical post-processing

Experiments plan

A first series of measurements had been performed on some tholins with a spectrogonio-radiometer to study their reflectance properties depending on the geometry. The spectrogonio-radiometer is an instrument that has been built in the laboratory and allows reflectance measurements in a wide spectral range in the visible and the infrared under various illumination and observation geometries (Potin et al., 2018). The main parameters we were interested in are the phase function as it would provide us information about the anisotropic property of the tholins reflectance and the single scattering albedo. Indeed, the SSA carries the spectral information (absorption bands) and describes the way the sample reflects the incident light back.

Investigating the phase function behaviour implies to perform reflectance measurements at different observation geometries. The more geometries we cover, the best the phase function is described. It is of course a trade-off between the number of geometries and the total experiments duration. For this first set of measurements, the following geometries had been considered: the emergent angle goes from -70 deg to 70 deg with a 10deg-step and this holds for incident angles of 0, 30 and 60 degrees respectively.

The reflectance measurements had been performed for the two different tholins provided by the LATMOS. As a reminder, the chemical compositions of the gas mixes that have been synthesised from are respectively 95% N_2, 5% CH_4, 500 ppm CO and 99% N_2, 1% CH_4, 500 ppm CO. As previously stated, the mismatch between MVIC data in the visible and pure tholins

spectrum which shows too dark colours has been highlighted in Grundy et al. (2018). In order to make the MVIC colours match with tholins spectrum, tholins needs to be diluted in some bright transparent ices. In order to experimentally study the effect of such a dilution process, dilution of pure tholins within some SiO has been conducted. Eventually, we ended with five different samples to measure, including the two pure tholins mentioned above, a dilution of 25% of pure tholins within 75% of SiO, same with 15% of pure tholins and idem with 5% of pure tholins.

Development of a numerical tool to post-process the results

From the reflectance we have measured under various geometries, we could deduce the single scattering albedo of the tholins. This could be interesting because it would allow us to plug it back in our Hapke model and therefore to conduct several tests.

The need for deriving the single scattering albedo of our tholins comes from the fact that none of the optical constants available in the literature seems to correspond to our Pluto's tholins (see Figure 12 which provides comparison between the spectra we got and the reflectances derived using Hapke's model from different set of optical constants found in the literature). We see that despite that they are synthesised under almost identical conditions and using the same experimental set-up, optical constants of Mahjoub et al. (2012) and Sciamma-O'Brien et al. (2012) do not match our reflectance measurements at all. On the contrary, although Khare et al. (1984) tholins match our spectra reasonably well, the major issue with those optical constants is their very poor spectral resolution and therefore the absence of any absorption feature.

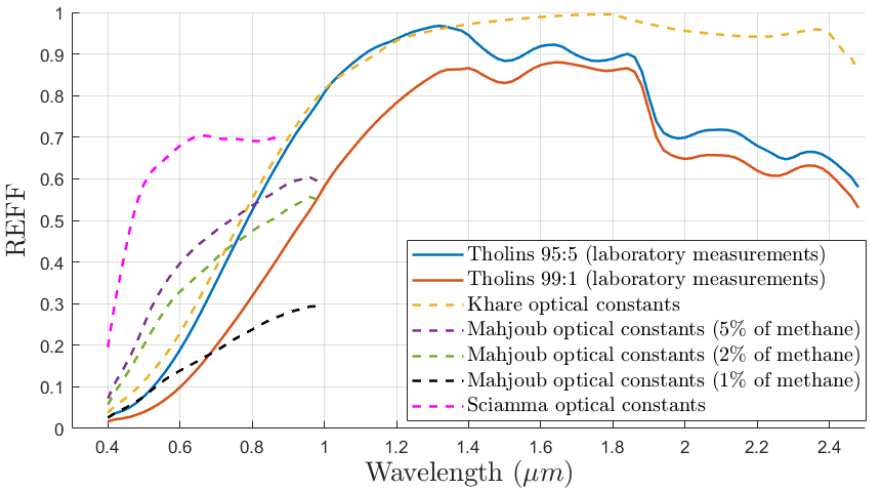

Figure 12: Comparison of the tholins spectra which have been measured in the laboratory with reflectance derived with Hapke's model from the optical constants available in the literature
In Hapke model, the porosity effect as well as the opposition effect have been neglected and the phase function has been assumed to be isotropic (meaning $P = 1$) for the sake of simplicity

This is why deriving the single scattering albedo from our experimental data by performing a model inversion could be useful. This step is not directly useful to investigate the relevance of tholins as potential analogues for the dark material on Pluto but it will lead to the creation of a powerful numerical tool for the rest of our work. For the sake of brevity and because the numerical aspect of this work will not provide any additional insight on the final purpose of it, this step will be presented only briefly. We will provide the main points of the method we used to perform this model inversion, as well as the results we have obtained. For the detailed equations and numerical implementation, the reader is referred to Appendix 14.3.

To inverse Hapke's model, a least-squares method has been considered as the easiest solution. However, as the model is quite complex, we first need to define which variables we want to retrieve. If we consider the complete form of Hapke's model, the reflectance is given by the following formula:

$$r(i,e,g) = K\frac{\omega(\lambda)}{4\pi}\frac{\mu_{0e}}{\mu_{0e}+\mu_e}\left[P(\lambda,g)B_{SH}(g) + H(w,\mu_{0e})H(w,\mu_e) - 1\right]B_{CB}(g)S(i,e,g,\bar{\theta}) \tag{9}$$

At this point, we really need to simplify the model and to make some assumptions to this end.

- The porosity parameter K was assumed to be constant and equal to 1. This means we are neglecting the porosity effects.
- The macroscopic rugosity Θ was assumed to be equal to 0. This aims at reducing the number of free parameters. Anyway, the addition of such a parameter would make the problem significantly more complex since the impact of Θ changes from one geometry to another and it could be very hard to distinguish this effect from the phase function effect. Last but not least, the shadowing function in which Θ appears is highly non linear and also extremely complex. Neglecting Θ would dramatically reduce the complexity of the inversion.

- We will neglect the opposition effect too. Indeed, it is important only for very small phase angles and we do not encounter such cases.

If the macroscopic rugosity parameter is set to 0, then the following relations hold $\Theta = 0 \rightarrow S(i,e,g) = 0$; $\mu_e = \cos(i)$ and $\mu_{0e} = \cos(e)$. The model is therefore reduced to:

$$r(i,e,g) = \frac{\omega(\lambda)}{4\pi} \frac{\mu_0}{\mu_0 + \mu} \left[P(\lambda, g) + H(w, \mu_0)H(w, \mu) - 1\right] \tag{10}$$

By inverting Hapke's model, we can deduce both the single scattering albedo which is a function of the wavelength only and the phase function which theoretically depends on both the wavelength and the phase angle g. However, we are facing an issue here since it is extremely difficult to distinguish the impact of the wavelength on the single scattering albedo from the impact of the wavelength on the phase function while looking at the evolution of the reflectance with the wavelength. This would be possible but it would complicate the problem since it would generate a huge number of unknowns (the phase function P depending both on λ and g, we would have unique value of P for each combination of λ and g). Furthermore, P can evolve with the wavelength but the dependency with respect to λ is not supposed to be very strong. As a result, we can quite safely assume that the phase function does not depend on the wavelength, which simplifies our model even more.

Once all these assumptions have been made, we have used a non-linear least squares method. However, because of the high non-linearity of the model, the non-linear least squares method was not able to converge while respecting the constraint which holds for the single scattering albedo (meaning $0 \leq w(\lambda) \leq 1$). This was due to the fact the first guess for $w(\lambda)$ was probably to far away from the actual solution to allow the least squares to converge. To make up for this issue, we have performed large Monte-Carlo simulations. Among those simulations, the one leading to the best result has been selected as the first guess for the least-squares method. This solution was very time-consuming but it has allowed the least-squares to converge. The results we finally obtained are provided below.

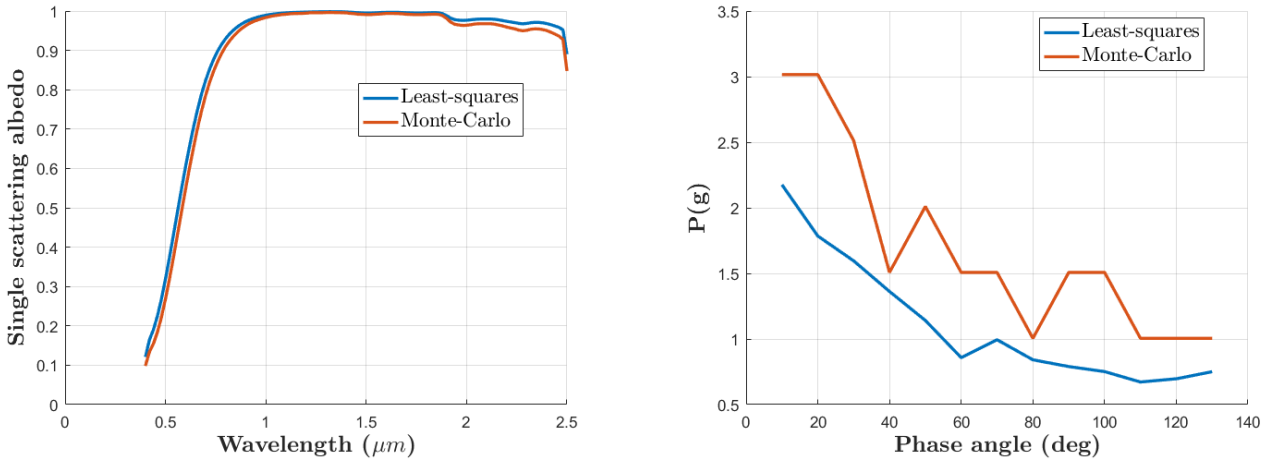

(a) Single Scattering Albedo w

(b) Phase function P

Figure 13: Results for the inversion of Hapke's model

In Figures 13a and 13b, the orange curves represent the outcome of the Monte-Carlo simulations which have been used as first guesses for the non-linear least-squares method while the blue curves represent the final outcomes of the least-squares. We see that for the single scattering albedo, the solution provided by the Monte-Carlo simulation is very close to that of the least-squares. Nevertheless, running the least-squares method is still necessary since the solution obtained with the Monte-Carlo technique has no reason to be converged.

The single scattering albedo and the phase function that have been derived from this inversion can now be used in the rest of our work as a modelling tool.

3.4.2 Reflectance behaviour as a function of the geometry

We first focus on the influence of the observation geometry. To this end, we plot the reflectance for different incident and emergent angles, and this is done for several given wavelengths. The aim is to highlight the way the sample reflects the incident light depending on the geometry.

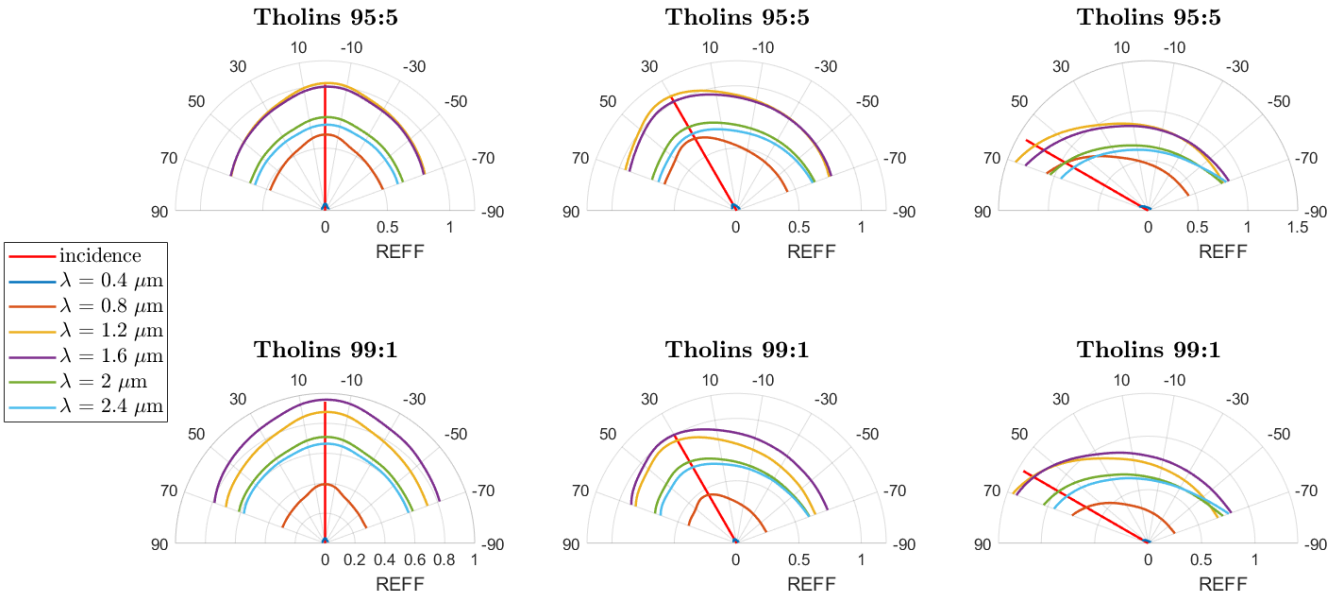

Figure 14: Tholins reflectance factor plotted as a function of the emergent angle, for different incidences and wavelengths *The two plots on the right corresponds to* REFF *measured for i = 0deg, the two plots in the middle to i = 30deg and finally the two plots on the left to i = 60deg.*

We clearly see that tholins tend to reflect the incident light backwards. In this particular case, it is hard to conclude about the reason of such a backscattering. As the particle size is extremely small (even smaller than the wavelength), it is very difficult to infer if the backscattering is due to the particle size or to its chemical composition. As we do not own any other sample characterised by such a small particle size, we cannot make a test aiming at identifying the reason of the backscattering.

This finding appears prima facie to be in contradiction with the fact that the material covering the dark regions of Pluto is characterized by forward-scattering (Grundy et al., 2018). However, in Grundy et al. (2018) a possible reason concealing these two contradicting observations is mentioned: tholins can maybe aggregate and therefore form larger particles which therefore behave as forward scatterers. This implies that the backscattering we have observed with our tholins would be due to the very small grain size rather than to their chemical composition.

3.4.3 Bands assignment

Looking at the three diluted tholins samples (blue, orange and yellow curves in Figure 15), we observe that the two absorption bands around 1.9 μm and 2.3 μm do not seem to depend on the tholins concentration. This probably indicates that these absorption features are not caused by tholins but rather by SiO. This could attest the presence of water in SiO or of some phyllosilicates mixed with pure SiO grains. Except for these two bands which are more probably due to SiO itself rather than to tholins, the spectra corresponding to diluted samples underline a strong spectral contrast attenuation compared to the pure tholins spectra. Even when 25 % of pure tholins are still present, the absorption bands we observe in the pure tholins spectrum are at least significantly attenuated or even undetectable. This is an interesting result too as it shows the tholins absorption bands might be barely detectable if tholins are indeed diluted in some bright ices as suggested in Grundy et al. (2018).

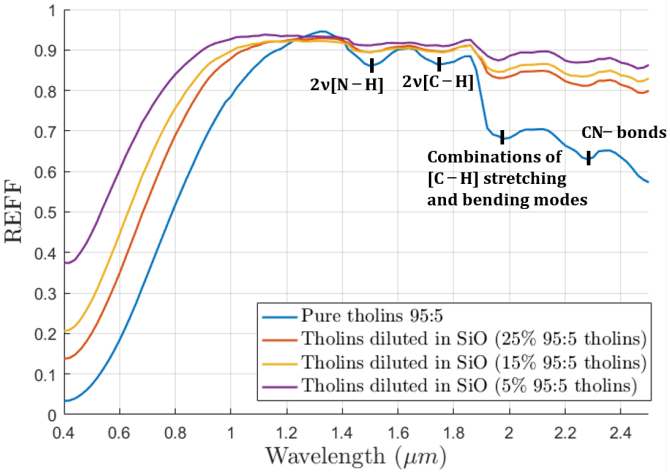

Figure 15: Tholins reflectance spectra with different dilution ratios (standard geometry: i = 0 deg, e = 30deg, Ψ = 0deg)

As mentioned before, Pluto's tholins were synthesised from an initial gas mixing which contained small amounts of CO in addition to the more widely used combination of N_2 and CH_4 (used for the synthesis of Titan's tholins). This aims at accounting for the presence of small quantities of CO in Pluto's atmosphere. We also have been provided with some Titan's tholins, synthesised in the exact same conditions as Pluto's tholins but not containing any CO. Comparing the reflectance spectra of the two types of tholins could help us assigning the absorption bands we have observed in Pluto's tholins (in case some bands only appear in Pluto's tholins, they would be likely to be due to the presence of CO in the initial gas mixture). Comparison between Pluto's and Titan's tholins is provided in Figure 16b.

Despite that we observe some differences in the reflectance levels between tholins with and without CO, we do not remark any clear difference spectrally speaking: the same absorption features appear in the spectra for both Pluto's and Titan's tholins. This advocates for assigning the tholins bands not to the presence of oxygen but rather to C-H and C-N bands. This result is in agreement with our expectations since the initial gas from which Pluto's tholins had been synthesised contained extremely small amounts of CO compared to N_2 and CH_4. Moreover, the bands we observed in the Pluto's tholins spectra had already been detected for different tholins (Roush and Dalton, 2004). The reflectance differences that we observe are likely to be due to differences in surface roughness or even in grain size distribution between Pluto's and Titan's tholins (the reflectance differences we observe being about 5% only).

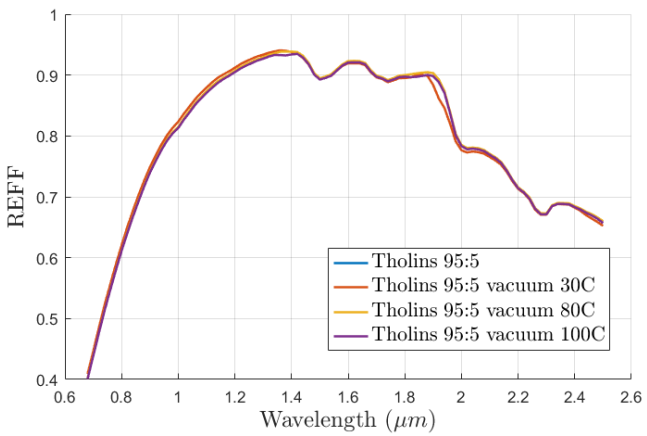

(a) Spectra of pure tholins under vacuum and undergoing a progressive heating process

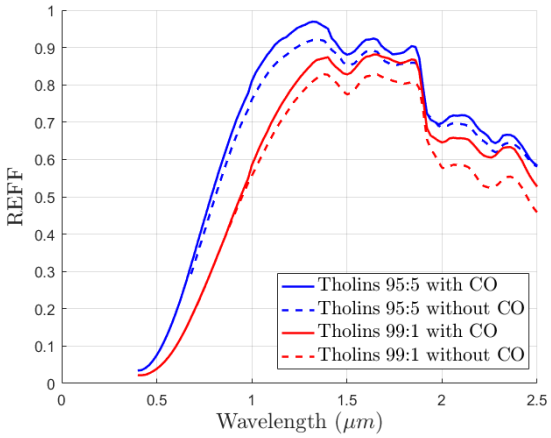

(b) Comparison between tholins with and without CO (Pluto's and Titan's tholins respectively)

The curves are hardly distinguishable from each other: there is no difference between the blue and the red ones and the yellow and purple ones are almost superposed to each other.

Figure 16: Results for the inversion of Hapke's model

Several absorption features had been detected in the two pure tholins spectra. The band toward 1.75 μm corresponds to 2ν[C-H] (first overtone). This band assignment is consistent with the fact that this band is deeper and wider for the tholins with 5% of methane than it is for the tholins with 1% of methane only. We indeed expect the tholins with 5% of methane to form more C-H bonds than the second one.

The absorption band around 2.25 μm - 2.3 μm is more likely due to some -CN bonds (first overtone as well). It could also correspond to some C-H harmonics but we do not see any significant difference in the band shape between the two different pure tholins, contrarily to the band toward 1.75 μm. This seems to be in agreement with the findings presented in Cruikshank et al. (1991) in which this band is assigned to -CN bonds rather than to C-H harmonics as proposed in Cloutis (1989).

The last two bands, around 1.5 μm and 1.9 μm - 2 μm respectively, seem to account for the presence of water which is likely to be absorbed by the tholins either during the measurement or even during the sample preparation. The assignment of those bands to water signatures is in agreement with Roush and Dalton (2004).

To examine the validity of the assignment of the 1.5 μm and 1.9-2.0 μm bands to some absorbed water, we have conducted reflectance measurements on the same sample but under vacuum (10^{-6} bar) and progressively heating the sample. Such a protocol aims at making the absorbed water, if any, evaporate. Therefore, if the two bands mentioned above are indeed caused by the presence of water, they would disappear or at least be strongly attenuated under the conjugate effects of vacuum and heat. The results we have obtained are presented in Figure 16a.

Comparing the tholins spectra in the nominal conditions (nominal pressure and temperature conditions) and under vacuum without any significant heating (T = 30°C), we do not see any difference. The band toward 2.0 μm is slightly modified between T = 30°C and T = 80°C (the change concerns its shape more than its depth). Again, we barely see any significant difference between the spectrum obtained at T = 80°C and that obtained at T = 100°C. However, the band around 1.5 μm does not change at all. These observations advocate against the prima facie assignment of these two bands to absorbed water. It seems that absorbed water contributes to a small extend to the band toward 2.0 μm but the band is mostly caused by an other compound.

Additional investigations on these two bands that we now know not to be due to absorbed water have led us to the following conclusions: the band around 1.5 μm is likely to be due to the first overtone of [N-H] bonds of primary and/or secondary amines whereas the 2.0 μm band appears to correspond to some combinations of [N-H] bending and stretching modes of primary amines (Workman, 1996).

3.4.4 Comparison with New Horizons data

Looking at MVIC spectral range, we remark a clear and strong impact of the dilution ratio in the visible: the higher the ratio of tholins is, the darker the sample is around 400 nm and therefore the steeper the red slope is. This is particularly interesting since it could help us to conclude about the dilution ratio using the MVIC data.

We now compare the reflectance spectra we have measured with the New Horizons data (see Figure 17). However, we need to keep in mind that we have not performed measurements at the exact same geometry as the one under which the New Horizons instruments had observed Pluto's surface and more precisely the Cthulhu region which is our region of interest. Figure 17 compares the New Horizons data with the laboratory reflectance measurements whose observation and illumination geometry was the closest to that of New Horizons.

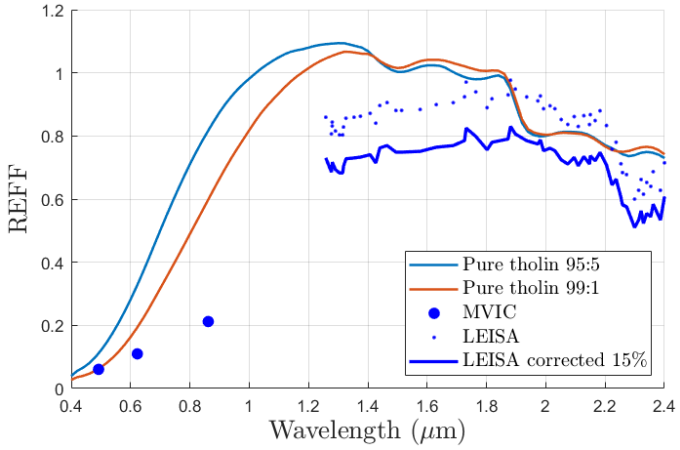

Figure 17: Tholins reflectance spectra measured in the laboratory, combined with New Horizons data

The blue dots correspond to the original New Horizons data whereas the blue line represents LEISA data corrected by an amount of 15%

Comparing New Horizons data with our laboratory measurements, we clearly see that the absorption bands present in tholins spectra do not appear in New Horizons spectrum. We observe that although the reflectance level of pure tholins seem to match MVIC colours quite well in the blue wavelengths, it is far too high in the rest of the visible spectral range. Pure tholins are too strongly pigmented to match MVIC colours. They are also too bright in the near-infrared compared to the corrected LEISA data. In addition to that, there is no spectral match between LEISA data and our reflectance spectra: the tholins spectral signatures do not appear in LEISA spectrum. On the contrary, the 2.3 μm is present in New Horizons spectrum only. This is rather consistent with the findings of the New Horizons data analysis performed before at the end of which we have concluded this band is more likely to attest for the presence of some hydrocarbon ices in Cthulhu than to be due to the dark material.

Looking back at Figure 15 again, we see that tholins diluted in SiO are too bright in the visible to match MVIC data.

However, we are still left with the fact that one of the main outcomes of the analysis of New Horizons data is that the red material present on Pluto's surface is spectrally transparent (or that its absorption features are not strong enough to be detectable among the instrumental noise of LEISA). This is in contradiction with the absorption features that have clearly been identified in tholins spectra.

Several reasons could explain a decrease of the spectral contrast, which might explain why the red material appears as being almost spectrally transparent in New Horizons data.

- First of all, the decrease of the spectral contrast could be explained by the radiolysis process (impacts by charged particles) which modifies the chemical composition of the surface. Radiolysis acting on carbonaceous compounds increases the length of the carbon chains and therefore darkens them (Cassidy et al. (2009), Johnson et al. (2004)). However, the darkening of tholins through radiolysis is not something we can investigate in the lapse of time of my internship (especially since it requires to ask for some experiment time in a particle accelerator). More researches will be conducted on this hypothesis after the end of my internship in GANIL (French acronym for Large Heavy Ion National Accelerator). Even if this hypothesis cannot be examined further here, it is worth noting that it will be explored in the near future.

- Another possible explanation for such a spectral contrast attenuation could be the impacts caused by micrometeorites (since Pluto has an extremely thin atmosphere). This phenomenon leads to a darkening of the surface and a decreasing of the spectral contrast too. This could therefore explain why the reflectance level in the near-infrared is lower for New Horizons data than for our laboratory spectra. The darkening hypothesis is easier to examine: we can indeed simulate the darkening of the surface caused by micrometeorites by mixing our Pluto tholins with a dark material (which is supposed to represent the dark material brought on by the meteorite). Our aim is to estimate how much dark material is needed to make the absorption bands we have observed in our Pluto's tholins spectra disappear. We would then be able to compare this value to the micrometeorites impacts rate in Pluto's orbital region to conclude about how realistic this hypothesis is.

- The last hypothesis is that the low spectral contrast could be due to porosity effects. Indeed, it has been shown (Poch et al., 2016) that post-sublimation residuals which form extremely porous structures indeed show lower spectral contrast than nominal samples. However, concerning Cthulhu region, it is hard to imagine that such sublimation processes could occur. Evidences for N_2 and CH_4 sublimation cycles on Pluto's surface have been brought on (Schmitt et al., 2017) but these sublimation cycles do not appear to involve Cthulhu region. This region is actually supposed to be depleted of N_2-ice (N_2 being too volatile to subsist in this part of Pluto) and the very small amount of CH_4 detected in Cthulhu are mainly located on mountains (no spectral evidences for CH_4 in the reddest parts of Cthulhu). It is therefore unlikely that the low spectral contrast is due to post-sublimation residuals. Nevertheless, high porosity effects as those characterising sublimation residuals could still occur and explain why tholins spectral features do not appear in New Horizons spectra. Indeed, because of their extremely small size and light weight and also because of the relatively weak gravity field exerted by Pluto, it is plausible that haze particles are deposited on Pluto's surface in such a way that they form very porous structures as well. This could produce materials behaving in a similar way as sublimation residuals do and thus explain the low spectral contrast we have observed in LEISA data. This last hypothesis will be investigated further in the coming months with an experimental protocol consisting in mixing tholins with ices, then making these ices sublimate in order to form porous sublimation residuals and finally measuring the reflectance spectrum of such a material. Again, this internship was not long enough to conduct such experiments but this hypothesis is still going to be tested.

3.4.5 Tholins darkening

We have decided to focus on the second hypothesis since it is the only one which could possibly be investigated during the rest of the internship (as it does not require to develop additional complex experiments). This hypothesis is also the only one which could explain both the low spectral contrast and the fact that our pure tholins are too bright in the near-infrared compared to LEISA data.
To examine this hypothesis, we have conducted a second series of measurements: starting from a pure tholin sample, we have progressively added some pyrrhotite (analogue for the dark material supposed to be brought by micrometeorites) to it to observe how the reflectance spectra change with different ratios tholins/pyrrhotite. To perform this pyrrhotite addition, the following experimental protocol has been followed:

- Addition to the required amount of pyrrhotite as darkening agent
- Use of a mortar to try mixing the tholins and pyrrhotite as homogeneously as possible
- Check of the apparent homogeneous aspect of the mixture with a binocular magnifying lens
- Reflectance measurement

The reflectance spectra with different amount of pyrrhotite have been measured with a fixed geometry (incidence equal to 0 deg, emergence set to 30 deg and azimuth to 0 deg (so phase angle equal to 30 deg)). However, this geometry differs significantly from that of the New Horizons observations. To be able to compare the spectra we got with those from the New Horizons instruments, we have to apply a correction to account for this geometry mismatch. The way this correction has been derived does not provide any additional insight here and is therefore presented in Appendix 14.4 only.

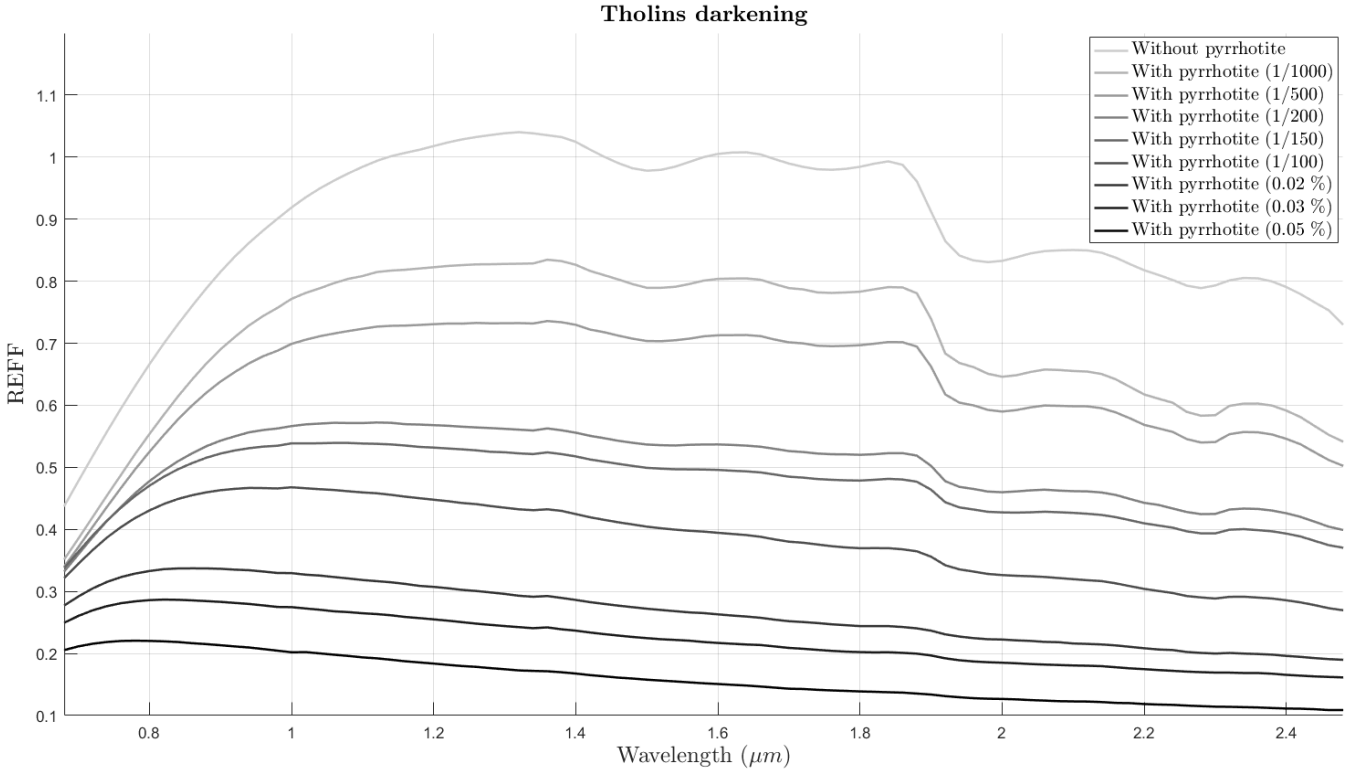

Figure 18: Tholins darkening with various amount of pyrrhotite (acting as a darkening agent)

As expected, the addition of a darkening agent lowers the global level: even extremely low amounts of pyrrhotite dramatically reduce the reflectance value. A pyrrhotite/tholins mass ratio of 1/200 is enough to make the reflectance level be divided by a factor 2. Moreover, the spectral contrast is also strongly attenuated by the addition of pyrrhotite. These two observations are in agreement with our expectations and confirm the fact that small quantities of darkening material are necessary to obtain dark spectrally-neutral tholins.

This is interesting since the analysis of New Horizons data has unveiled the fact that Pluto's dark material does not make any spectral features appear in New Horizons spectra. As expected, the addition of a darkening agent to pure tholins not only induces a attenuation of the spectral contrast but also leads to a strong decreasing of the reflectance level which might be consistent with the reflectance level measured by LEISA.

Concluding points

- Our tholins show very strong backscattering, likely to be due to their small size (below the wavelength). Forward scattering observed in Cthulhu (Grundy et al., 2018) can be explained by the formation of aggregates.
- Tholins bands have been assigned: 2ν[N-H] (1.5 μm), 2ν[C-H] (1.75 μm), [C-H] stretching and bending modes (1.9-2.0 μm), CN- bonds (2.3 μm).
- The absence of tholins bands in New Horizons spectra can be explained by an attenuation of the tholins spectral contrast, for which three hypotheses have been made: radiolysis, porosity effects and meteorites impacting. The last one has been tested by darkening tholins with pyrrhotite. As expected, this has induced an attenuation of the spectral features but also a decrease of the reflectance.

3.5 Optimisation process to determine Cthulhu's surface composition

Summarising the main concluding points we have obtained so far:

- New Horizons spectra in Cthulhu region do not show any spectral feature which seems to be assigned to the presence of the dark material. The 2.3 μm is more likely to be due to the presence of hydrocarbon ices. It appears that the red material is not present as a pure material on Cthulhu but rather is mixed with water and/or hydrocarbon ices.
- On the contrary, the tholins spectra we have measured present several absorption bands. Several hypotheses have been proposed to explain the attenuation of the spectral contrast (radiolysis, micro-meteorites impacts, tholins forming very porous structures on Pluto's surface). The mixing of tholins with a darkening agent (pyrrhotite) to model the effect of micro-meteorites impacting has been tested, the problem being that the lowering of the spectral contrast it induces also comes with a decreasing of the global reflectance level. This might explain the fact that LEISA spectra show lower reflectance level than what we have obtained measuring the reflectance of pure Pluto tholins.

Based on these observations, we have tried to model Cthulhu reflectance spectrum in order to match LEISA spectrum as well as possible. This was done in the continuity of the work performed in Cook et al. (2018), the aim being to determine the composition of Cthulhu surface that best fits the New Horizons LEISA. In Cook et al. (2018), the surface had been modelled as a spatial mixture (see Appendix 14.2 for more details) between two units, one composed of the refractory species (namely water ice as well as C_2H_4, C_2H_6, C_3H_8, CH_3OH ices and tholins) and the other one covered with CH_4-ice. The refractories are mixed together in an intimate mixture (see Appendix 14.2). The diameters and mass fractions were left as free parameters of the optimisation process, as well as the spatial ratio between the refractories and the volatiles units. In Cook et al. (2018), this had been done not only for Cthulhu region but for various Pluto's terrains, most of them being characterised by clear ices spectrum.

Concerning Cthulhu region particularly, the main problem of the work presented in Cook et al. (2018) is that the optimisation algorithm had looked for the lowest χ^2 between the modelled reflectance and New Horizons spectrum using LEISA spectral range only. This means that the reflectance behaviour in the visible has not been taken into account in the optimisation process. The problem arises from the fact that Cthulhu region shows a very red slope (the reflectance being very low in the visible and very high in the infrared), which is not the case of most of other Pluto's regions mainly covered by ices. The main difference between the optimisation process we have conducted and the work presented in Cook et al. (2018) is therefore the addition of MVIC data in the calculation of the χ^2. The purpose of it is to add constraints on the reflectance level in the visible, since this would directly constrain the required amount of tholins. If we only consider LEISA data, we might end up with very high reflectances in the visible, due to the presence of water and hydrocarbon ices. MVIC data have been weighted in such a way that the three MVIC channels together weight as much as LEISA data do but proportionally with respect to the spectral range MVIC and LEISA respectively cover.

Keeping in mind the concluding points mentioned above, it has appeared that pursuing this optimisation work could be very interesting. Indeed, the analysis of New Horizons data has led us to think that tholins are mixed with some water and hydrocarbon ices as suggested by Cook et al. (2018). In addition to that, since we have directly measured the reflectance of Pluto tholins, we could use the single scattering albedo derived from our laboratory measurements for tholins, whereas the same optical constants as those used in Cook et al. (2018) for ices have been plugged in. As explained before, and because we are especially interested here in the dark material, we have considered MVIC data in addition to LEISA data in the optimisation process.

The simplified Hapke model described in Cook et al. (2018) has been used again. As the reminder, the simplified version of Hapke's model is provided in Equation 11.

$$r(i,e,g,\lambda) = \frac{\omega(\lambda)}{4\pi}\frac{\mu_0}{\mu_0+\mu}\left[P(g,\lambda)B_{\mathrm{SH}}(g) + H(\mu_{0e})H(\mu_e) - 1\right] \tag{11}$$

where the phase function is assumed to be isotropic ($P(g,\lambda) = 1$) and the opposition effect is modelled as follows:

$$B_{SH}(g,\lambda) = 1 + \frac{B_0(g,\lambda)}{1+(1/h)\tan(g/2)} \text{ with } B_0(g,\lambda) = \frac{S(0)}{\omega(\lambda)P(0,\lambda)} \tag{12}$$

$S(0)$ refers to the specular component of the particle scattering function and is derived from the optical constants as:

$$S(0) = \frac{(n-1)^2+k^2}{(n+1)^2+k^2} \tag{13}$$

So that we end up with:

$$\Rightarrow r(i,e,g,\lambda) = \frac{\omega(\lambda)}{4\pi}\frac{\mu_0}{\mu_0+\mu}\left[\frac{B_0(g,\lambda)}{1+(1/h)\tan(g/2)} + H(\mu_{0e})H(\mu_e)\right] \tag{14}$$

To help the algorithm converging and to slightly simplify the model compared to the one used in Cook et al. (2018), a limited number of possible compounds has been provided to the numerical model. For each of these components, its mass ratio and the mean diameter of the particles have been left as free parameters. The chemical components that have been selected to be plugged in the model are: crystalline H_2O-ice, C_2H_6-ice, CH_3OH-ice, tholins and CH_4-ice.

As it was already the case in J. Cook (2018), H_2O, C_2H_6, CH_3OH and tholins are forming an intimate mixture (containing all the refractories) which is itself spatially mixed with CH_4-ice. As an additional constraint to our model, the particle diameters are free parameters but can only take values between 0.1 and 100 μm.

As previously stated, this optimisation process has been performed using the single scattering albedo derived from our measurements. This was done not only with pure tholins but also for darkened tholins (addition of small amounts of pyrrhotite was used for the darkening). This aimed at concluding whether darkened tholins fit the New Horizons spectra better than pure tholins do.

Concerning the optimisation process itself, it is described with more details in Appendix 14.5 but we will present it briefly here. Several optimisation algorithms have been tested (among which genetic, differential evolution and predator/prey algorithms). A simple genetic algorithm has been selected as the best performing one for this particular problem. As a brief description of this algorithm, it is based on Darwin's natural selection principle applied to a population of solutions in which each solution (modelled reflectance for a given set of parameters) is associated with a "fitness" (meaning the corresponding χ^2 with respect to New Horizons data). The solutions with the lowest fitness are selected as the "best individuals" of the population and the next

generation is derived from these selected individuals. At the end, the algorithm eventually converges toward the best individual (which actually corresponds to the best set of parameters to minimise the difference between the model and New Horizons data).

The optimisation algorithm has been re-run several times with different initial random seeds to verify that is has reached global convergence (and has not gotten stuck on a local optimum).

Below are provided some of the best results we have obtained among the different configurations we have tried, for both Cthulhu spectrum showing few evidences for the presence of H_2O and H_2O-rich region on the contrary. The detailed results in terms of fitness values and estimation of the best sets of free parameters can be found in Appendix 14.5.2.

3.5.1 Results with LEISA data only (as a means of validation with respect to the work presented in Cook et al. (2018))

If we only consider LEISA data (and not LEISA + MVIC as previously stated), our model does not match New Horizons spectrum as well as it does in Cook et al. (2018) (the differences are higher, probably because of the simplified model we have used) but the global shape of the optimised model is similar between our work and that presented in the paper.

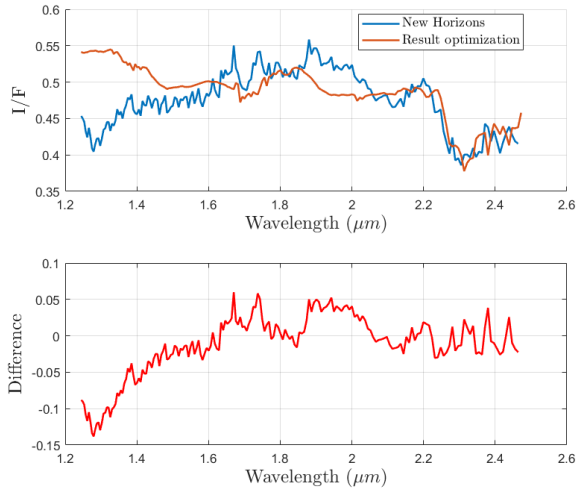

(a) only LEISA spectral range

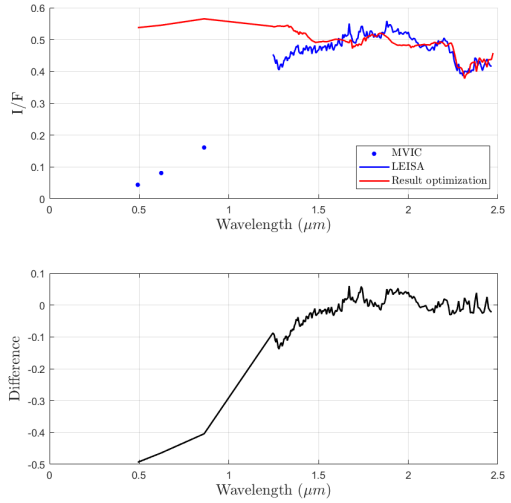

(b) Extension of the model to MVIC spectral range

Figure 19: Pure tholins (w/o pyrrhotite) - no correction for LEISA data (optimisation based on the fitness with respect to LEISA data only)

Still, one important issue is that even if the optimisation algorithm is able to match more or less precisely LEISA data, if we extend the spectral range to the visible, we do not see any reflectance decreasing. This proves that we really need to consider both LEISA and MVIC data if we want to model Cthulhu's reflectance in a realistic way. As explained before, we expect MVIC data to bring much more constraints on the required amount of tholins since tholins are the only component presenting such a red slope in our model. In the following, each optimisation has been performed considering both LEISA and MVIC data (weighted as explained in the introduction).

3.5.2 Results of the first optimisation model

Using the reflectance model previously described, we have run the algorithm for the two tholins samples we have been provided with (5% and 1% of methane respectively) and for different darkening ratios for each of these two samples. Below are only provided the best results for the two kinds of tholins (meaning that we will only present the results for the darkening ratio leading to the lowest difference with respect to the New Horizons data). Detailed results of our optimisation process (both χ^2 values and estimated free parameters) are provided in Appendix 14.5.2.

In both cases (tholins with either 5% or 1% of methane), the best fit is obtained with pure tholins, without any darkening pyrrhotite. This proves that if we do not use only tholins but we rather mix them with hydrocarbon and water ices, the first conclusion we drew about tholins being too bright in the nearinfrared and therefore requiring to be darkened is not valid anymore. The hypothesis of tholins darkening by meteorite impacting to explain the disappearing of tholins bands is therefore not correct since this would also induce a lowering of the photometry level which is not required here to match New Horizons data.

Looking at the H_2O-rich region of Cthulhu, we see that the spectrum obtained with 95:5 tholins shows a relatively good match with respect to LEISA data in the near-infrared (see Figure 20a). However, the red slope in the visible we have obtained with our best fit model presents significant differences compared to the one deduced from MVIC data. The shape of the red slope is determined by that of the tholins (as none of the other components shows such a red slope in the visible). Thus, being able to match MVIC data is of major importance here to identify the red material covering Cthulhu region.

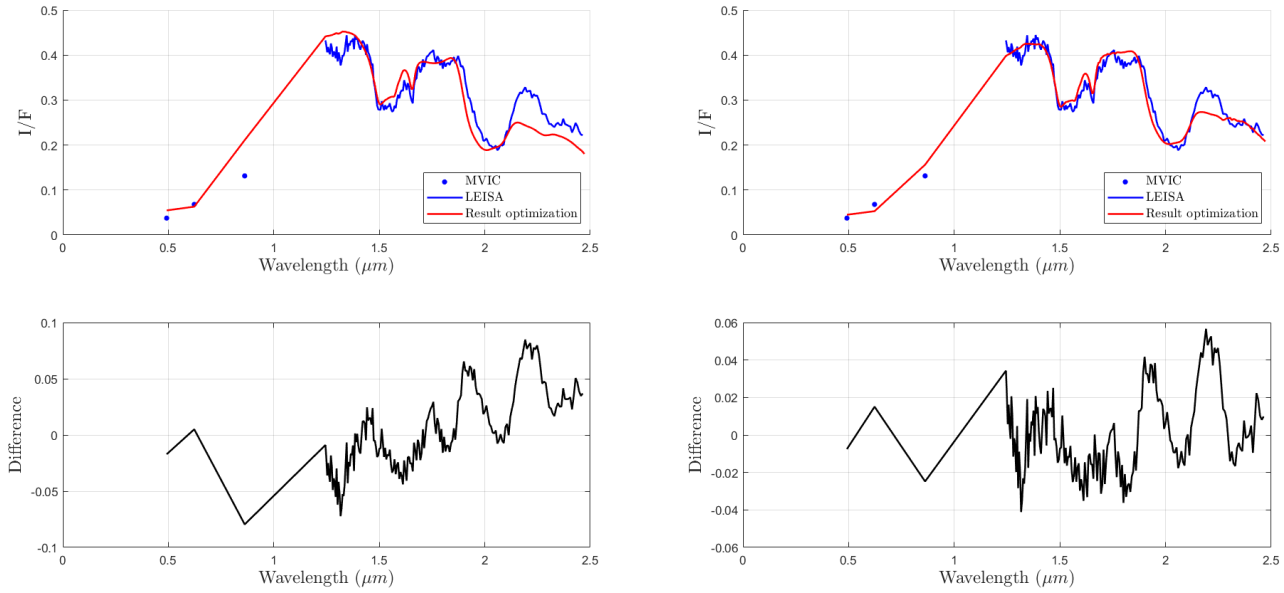

(a) Pure tholins 95:5

(b) Pure tholins 99:1

Figure 20: Optimisation results for H_2O-rich region

Changing the tholins composition from 5% of methane to 1% significantly improves the match between our model and MVIC values in the visible (see Figure 20b). The red slope of our model is clearly closer to that of MVIC data, even if the match is not perfect yet. This result is consistent with what we could expect as tholins with only 1% of methane are more plausible to form in Pluto's atmosphere than those with 5% of CH_4 (N. Carrasco, T. Gautier (personal communication, 2018)). In the near-infrared, there is no major difference in the quality of the fit for the two tholins compositions.

The presence of the two H_2O absorption features (around 1.5 and 2.0 μm) strongly helps the optimisation algorithm to reproduce the New Horizons spectra. Indeed, it provides additional clear constraints on the photometry level making the spectra easier to reproduce.

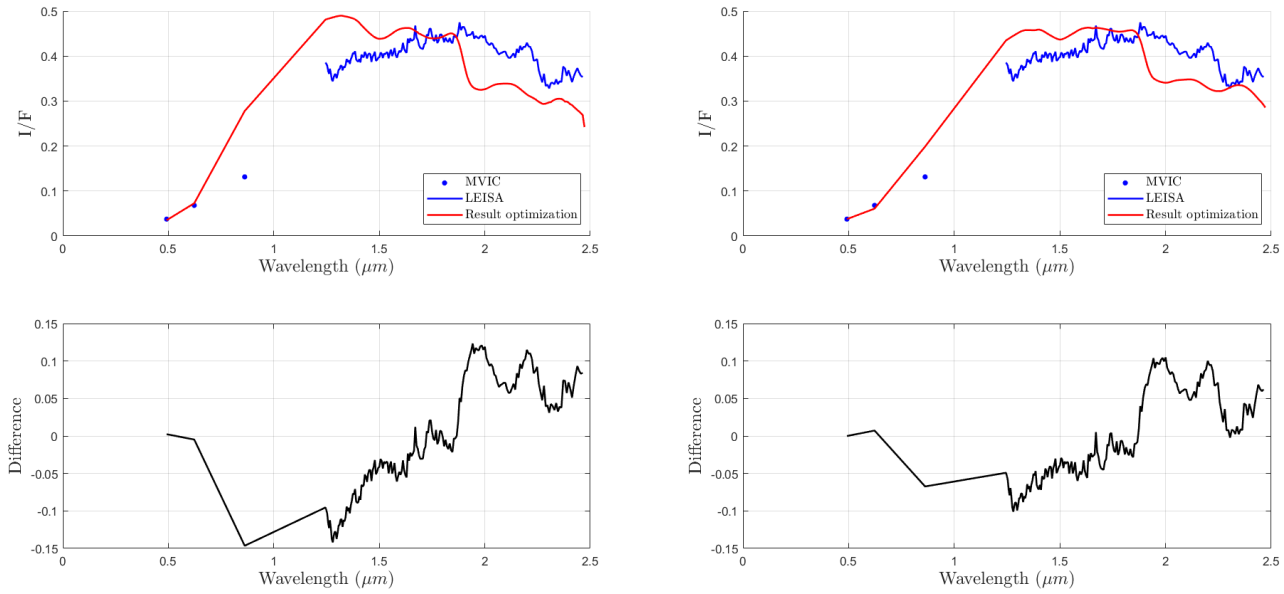

(a) Pure tholins 95:5

(b) Pure tholins 99:1

Figure 21: Optimisation results for H_2O-poor region

Now looking at the results we obtained for the H_2O-poor region of Cthulhu (see Figures 21a and 21b), we see that the optimisation algorithm does not manage to fit the New Horizons spectrum when there is no clear signatures for H_2O-ice absorption. There are two main reasons which can explain such a low-quality fit. The first one is simply the fact that the two H_2O bands are not present and the spectrum is therefore significantly less constrained, as already stated. Moreover, as mentioned during the analysis of the New Horizons data, the red material is almost spectrally transparent in LEISA data. However, as our best fit has been obtained with pure tholins rather than darkened ones (so the spectral contrast is not attenuated), our tholins spectrum still presents a decreasing in reflectance around 1.9-2.0 μm as well as the absorption feature toward 2.3 μm. We have to keep in mind that despite the poor match in the near-infrared, the detection of the presence of tholins by the model is imposed because of the red slope in the visible. These two remaining spectral features make the reflectance level lower than that of LEISA data and therefore the optimisation algorithm does not see the point in adding hydrocarbon ices to reproduce the absorption band toward 2.3 μm since the reflectance level of our model is already lower than what it should be around 2.3 μm.

The results the optimisation algorithm has provided us with highlight the need for complementary work to obtain a better fit in the near-infrared and to further investigate the absence of tholins spectral features in New Horizons data. Apart from the darkening of tholins caused by meteorites impacting (which is apparently not needed according to our optimisation results), two other hypotheses have been envisioned to explain the attenuation of the tholins absorption bands, namely the effect of radiolysis and the possible consequences on the spectrum of tholins forming highly porous structures on Pluto's surface. These two hypotheses still need to be explored, in order to see if their effects can possibly suppress the tholins absorption features and therefore help the optimisation algorithm to reproduce LEISA spectra. It could also be very interesting to observe how much the red slope in the visible evolves once the tholins have experienced radiolysis.

3.5.3 Results of the second optimisation model

So far, the model we have used was based on that presented in Cook et al. (2018). However, N. Carrasco (personal communication, 2018) and L. Panayotis (personal communication, 2018) have indicated us that this model might not be the most representative one considering the way tholins are thought to form in Pluto's atmosphere. Instead of assuming tholins are intimately mixed with ices, it is more likely that ices actually condensate around tholins particles. The model exposed in Grundy et al. (2018) would therefore be more relevant to model the composition of Cthulhu surface. This model has been described in section 3.3.4 but, as a reminder, it assumes that grains are composed of a core tholin surrounded by condensed ice (tholins act as pigments and ices form the surrounding matrix).

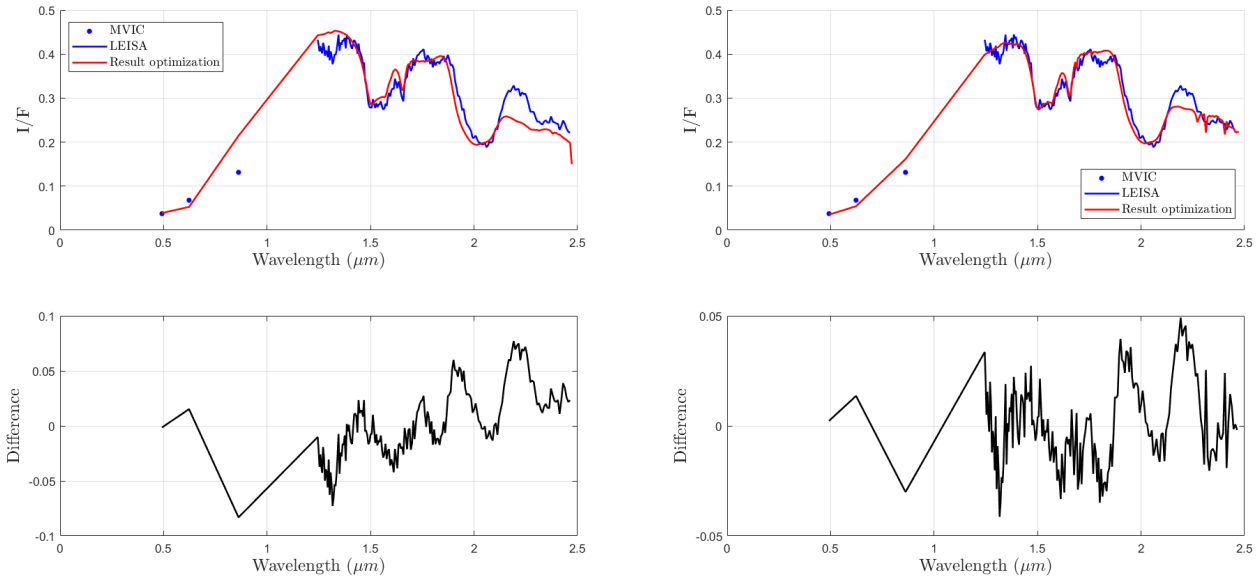

(a) Pure tholins 95:5

(b) Pure tholins 99:1

Figure 22: Optimisation results for H_2O-rich region

When we tried to further investigate the work presented in Grundy et al. (2018) (see section 3.3.4), we have observed that ices absorption bands tend to appear in the spectrum and that it was impossible to match both MVIC and LEISA data with such a model. Nonetheless, we can still try to apply this more realistic model here and see if we still encounter the difficulties we have just mentioned. We have some advantages here compared to the preliminary work performed in section 3.3.4. First, we can directly use the tholins single scattering albedo we have measured instead of optical constants found in the literature. Moreover, using our optimisation model, we have many more free parameters than what was the case before (only the fraction of tholins per grain and the grain size were left as free parameters then). Leaving many parameters as free in our model might help us to find a better match with respect to New Horizons data and to avoid the two obstacles previously identified (presence of ices bands and mismatch between MVIC and LEISA data).

To better characterise our new optimisation process, we will briefly describe the assumptions and choices we made. We are considering only H_2O, C_2H_6 and CH_3OH as the ices that can possibly condensate on tholins in the atmosphere. The model considers two units: the first one composed of ice grains with tholins inside. These ice grains are intimately mixed together. The second unit is composed of CH_4-ice, to account for the eventual presence of methane ice in the bedrock of Cthulhu. Basically, the only difference between this new model and the previous one is that tholins are not intimately mixed with H_2O, C_2H_6 and CH_3OH ices but rather captured inside these icy grains. Therefore the free parameters are the following ones: diameters of H_2O, C_2H_6 and CH_3OH icy grains, fraction of tholins inside icy grains, mass fractions of H_2O, C_2H_6 and CH_3OH ices in the intimate mixture they form and spatial ratio between the two units we have just described. This second model has been implemented in Tudat as well and the same optimisation algorithm and settings have been used. The results we have obtained are provided below in Figures 22a, 22b, 23a and 23b. Again, detailed results of our optimisation process for this second model can be found in Appendix 14.5.

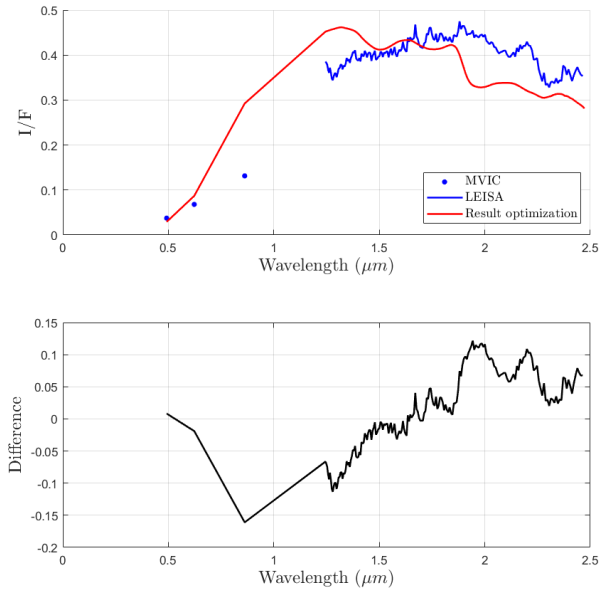

(a) Pure tholins 95:5

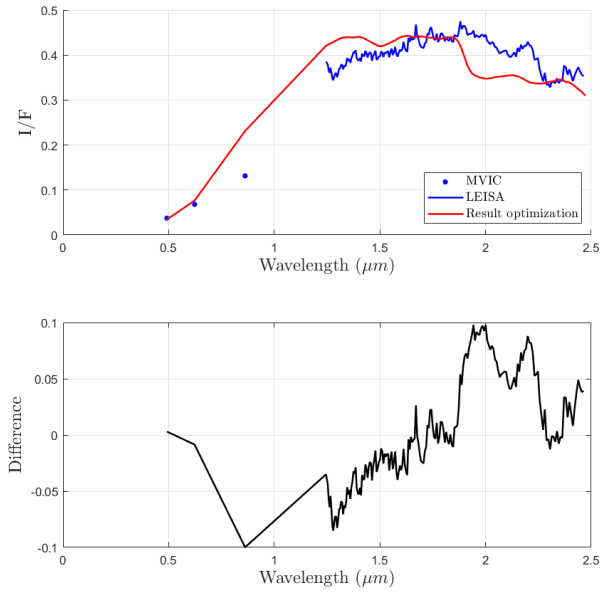

(b) Pure tholins 99:1

Figure 23: Optimisation results for H_2O-poor region

The global results are similar to those obtained with the first model (poor match in H_2O-poor region because of the remaining tholins bands, pretty good match in H_2O-rich region, which proves we manage to reproduce the photometry level quite well by using pure tholins rather than darkened ones). The only difference is that the fit is slightly better (for every case) with the second model which is also thought to be more plausible to be representative of what occurs on Pluto. As this condensation phenomenon of hydrocarbon ices on tholins particles is really expected to happen in Pluto's atmosphere, it is a good sign that we are still able to match the photometry level reasonably well with this model based on the condensation of ices on core tholins. Some deeper investigations on the consequences of radiolysis and porosity effects on the attenuation of tholins bands is still required to match New Horizons spectral features in the near-infrared (as it has already been highlighted by the first model).

Concluding points

- Using our optimisation model which adds hydrocarbon ices to tholins while leaving mixing ratios and grain sizes as free parameters, we have managed to reproduce the photometry level of New Horizons spectra reasonably well with pure tholins (worse fit with darkened tholins). This has proved the darkening of tholins by meteorites impacting is not the correct hypothesis to explain the attenuation of tholins spectral features.
- However, the presence of tholins bands in our modelled spectra while they do not appear in New Horizons ones is a problem we still need to address. This is why additional investigations on bands attenuation through radiolysis and/or porosity effects are required.
- Darker tholins (synthesised from an initial gas mix with 1% of methane only instead of 5%) has led to a better fit with New Horizons data, which is a good sign since these tholins are considered as more likely to form in Pluto's atmosphere.
- Globally, the model based on ices condensed around core tholins (which is thought to be more plausible to be representative of what occurs in Pluto's atmosphere) has provided slightly better fit than the model based on tholins intimately mixed with ices.

4 Outcomes

The work performed leads to a better characterisation of Pluto tholins. The SEM analysis provided us with a good estimation of the tholins mean diameter (about 400 nm) while successive reflectance spectra measurements have helped us to conclude about the bands assignment: 4 bands have been observed in tholins spectra and were assigned to bonds between C, N and H atoms (this finding being consistent with the results of the mass spectroscopy study conducted in LATMOS (N. Carrasco (personal communication, 2018))). One of the main outcomes of our reflectance measurements under various geometry configurations is that our tholins show a strong backscattering, likely to be explained by the very small size of tholins grains (lower than the wavelength).

The analysis of the New Horizons data in the near-infrared retrieved by the LEISA instrument has not allowed us to conclude about the band toward 2-2.1 μm we observe in Cthulhu region. It can be partially explained by water ice but there is also a contribution to that band which is not related to H_2O. We have not been able to conclude about it (additional work to deconvolve these two bands would be required). Nevertheless, this analysis has provided us additional insight about the strong 2.3 μm band, which was first thought to be due to the presence of the dark organic material. It has appeared that this band is much more likely to be caused by hydrocarbon ices such as C_2H_4, C_2H_6, C_3H_8, CH_3OH...

The comparison between the New Horizons spectrum (corrected to account for the calibration issues) and the spectra we have measured in the laboratory have risen an major issue. Indeed, the four absorption bands we have identified in the tholins spectra we have measured are not detectable in LEISA spectrum. Several hypotheses have been considered to explain such a low spectral contrast for Pluto's dark material. This can possibly be explained by the effect of radiolysis (impacting by charged particles) which tends to darken carbonaceous materials and to chemically modify the surface. The attenuated spectral contrast can also be due to the darkening of the surface caused by meteorites impacting. Another hypothesis is that once formed in Pluto's atmosphere, tholins are deposited onto the surface in highly porous structures. High porosity can significantly attenuate the absorption features and can therefore play a role here too.

Because of the limited duration of this internship, only the darkening of tholins due to meteorites impacting has been further investigated. Tholins have been mixed with pyrrhotite acting as a darkening agent (different pyrrhotite/tholins ratios have been tested). We have measured reflectance spectra of those mixes in order to see if they could better match the New Horizons data. It is worth noting the two other hypotheses are going to be examined in more details in the near future.

In parallel of the laboratory measurements of tholins spectra, we have developed a numerical technique to retrieve the single scattering albedo and the optical constants from the spectra we measured under different geometries of observation and illumination. This is extremely useful since tholins optical constants available in the literature show strong differences depending on the way they are synthesised (different optical constants are even sometimes available for the same sample because they have been measured with different methods). Having developed this method has been of great interest in the rest of our work because we have been able to directly use the optical constants of our tholins which we know to be synthesised in conditions close to how tholins are expected to form in Pluto's atmosphere.

Finally, we have made use of the conclusions drawn at the end of our analysis of New Horizons data and of the tholins optical constants we have derived from our laboratory measurements (for both pure and darkened tholins) to try to reproduce the New Horizons spectrum measured in Cthulhu region. We have based our work on that presented in Cook et al. (2018), the main difference being that we are interested in the identification of the red material covering Cthulhu. Therefore, we have not only used LEISA data (in the near-infrared) as done in Cook et al. (2018) but also MVIC data (visible) to better estimate the role of tholins if any (since tholins present a strong red slope in this spectral range). We have used an optimisation algorithm trying to minimise the χ^2 between our model and New Horizons spectrum and then providing us with the corresponding best set of parameters. It could therefore give us good estimation of the mass ratio of tholins present in Cthulhu region, as well as identify which of the ices mentioned as potential candidates for the 2.3 μm band in LEISA spectra are the most plausible ones.

The optimisation algorithm has succeeded in reproducing Cthulhu spectrum in regions containing more H_2O-ice. This is a very interesting result since it shows we have been able to reproduce the photometry level of New Horizons data reasonably well, especially with darker tholins (1% of methane only in the initial gas composition from which tholins are synthesised, which is a gas composition estimated to be more plausible than the one with 5% of methane in Pluto's atmosphere). The optimisation process has also led us to conclude that tholins darkening is not required to match New Horizons data and actually leads to worse fits if we choose to consider it. This has allowed us to state that our hypothesis about spectral attenuation due to meteorites impacting is not the correct one. In addition to that, our model using condensed ices around core tholins has led to better matches than the one using tholins intimately mixed with ices. This is a good sign as well because this condensation phenomenon is thought to be very likely to occur in Pluto's atmosphere.

However, our optimisation process has not managed to reproduce New Horizons spectrum very well in the regions of Cthulhu with low amounts of water ice. The lack of spectral constraints was one the major issues we have encountered. Moreover, some absorption features for tholins are still present while they do not appear in LEISA data (even for darkened tholins). This has highlighted the need for deeper investigations on the origin of the absence of tholins bands in New Horizons data. As already mentioned, two remaining hypotheses are still to be explored to try to better fit the data.

The optimisation process developed during this internship can be used again after the future experiments are conducted to see if it is then possible to reproduce New Horizons spectra, even in regions with few water-ice.

5 Conclusions

The initial purpose of this internship was to conclude about tholins being good analogues for the dark material covering parts of Pluto's surface or not. The comparison between our model, based on laboratory measurements performed during the internship, and New Horizons data has not been conclusive enough to answer this question. The remaining presence of tholins absorption features in our modelled spectrum whereas there is no trace of these bands in LEISA data advocates against the identification of tholins at prima facie. However, tholins are still the only material we have been able to envision as analogue for Pluto's dark material (considering the red slope it shows in the visible and the plausibility of such organic materials to be produced in Pluto's atmosphere, as it is the case on Titan). Nonetheless, this internship has allowed us to further characterise the spectral behaviour of tholins and to raise some questions and research avenues. We should keep in mind that two of our hypotheses are still to be tested to explain the absence of those absorption bands in New Horizons spectra (see section 6).

The numerical tools developed during this internship (numerical technique to retrieve the single scattering albedo and the optical constants from laboratory measurements as well as the optimisation algorithm) can be used once the experiments testing these two hypotheses are conducted.

The optimisation process we have developed will be able to conclude about how well we manage to fit the data with our model. Depending of the results we will obtain at the end of the experiments conducted to investigate the effects of radiolysis and high porosity, we will probably be able to conclude more precisely about the relevance of tholins as analogues for Pluto's dark material.

6 Recommendations for future work

As previously explained, this internship has not led to a clear conclusion about the identification of tholins in Cthulhu region. We still have some discrepancies between our model (using tholins as analogue for the red material) and New Horizons data. However, some hypotheses made during this work remain to be examined:

- The effect of radiolysis (impacting by charged particles) has to be investigated. Indeed, the radiolysis phenomenon chemically modifies the surface and might therefore explain the darkening of tholins, as well as the absence of tholins absorption bands in New Horizons spectra. This hypothesis is planned to be tested in the coming months by exposing tholins to accelerated heavy ions in GANIL (French acronym for Large Heavy Ion National Accelerator).

- High porosity effects have also been envisioned as a possible explanation for the attenuation of the tholins spectral contrast (as tholins can plausibly be deposited onto Pluto's surface in such a way that they form highly-porous structures). It has been proved (Poch et al., 2016) that such porous structures are characterised by a significant attenuation of their absorption bands. In order to verify the relevance of this hypothesis, tholins will be mixed with ice. Then this ice will be sublimated to form post-sublimation highly porous residuals whose reflectance can be measured.

The results obtained at the end of these two experiments can be used in the optimisation process developed during this internship to conclude about whether or not we got results closer to that of New Horizons. In addition to these two additional laboratory experiments, more complex models can also be tested in the optimisation process. So far, only relatively simple models have been used with only few types of ices (H_2O, C_2H_6 and CH_3OH). HCN-ice has been mentioned as being likely to form and condensate on tholins in Pluto's atmosphere (N. Carrasco (personal communication, 2018) and L. Panayotis (personal communication, 2018)). The only reason why we have not incorporated it in our model is that we do not have access to optical constants for HCN-ice. If these optical constants are available in the near future in our spectral range of interest, it could be interesting to add them in our model to see if it improves the fit or not. Any other potential candidates can of course be added in the optimisation process, keeping in mind that the more free parameters we have, the more difficult it becomes for the optimisation algorithm to converge.

Additional work also remains to be done on New Horizons data, in particular the identification of the 2.1 μm band present in Cthulhu region. This band is probably not only due to the presence of water-ice but additional analysis is required to decoupled this band from the H_2O 2.0 μm band.

Most of the points listed above are going to be examined further in the near future but it was not possible to do it within the duration of this internship. They should provide us more insights about the points that remain unclear and hopefully help us to conclude about the identification of tholins as the dark material on Pluto.

7 References

Brasse, N., Munoz, O., Coll, P., and Raulin, F. (2015). optical constants of titan aerosols and their tholin analogs: experimental results and modeling/observational data. *Planetary and Space Science 109-110*, pages 159–174.

Cassidy, T., Coll, P., Raulin, F., Carlson, R., Johnson, R., Loeffler, M., Hand, K., and Baragiola, R. (2009). Radiolysis and photolysis of icy satellite surfaces: Experiments and theory. *Space Science Reviews 153*, pages 299–315.

Cloutis, E. (1989). Spectral reflectance properties of hydrocarbons: Remote-sensing implications. *Science 245*, pages 165–168.

Cook, J., Dalle Ore, C., Protopapa, S., Binzel, R., Cruikshank, D., Earle, A., Grundy, W., Ennico, K., Howett, C., Jennings, D., Lunsford, A., Olkin, C., Parker, A., Philippe, S., Reuter, D., Schmitt, B., Singer, K., Stransberry, J., Stern, S., Verbiscer, A., Weaver, H., Young, L., Hanley, J., Alketbi, F., Thompson, G., Pearce, L., Lindberg, G., and Tegler, S. (2018). The distribution of h2o, ch3oh and hydrocarbon-ices on pluto: analysis of new horizons spectral images. *Icarus submitted*, page TDB.

Cruikshank, D., Allamandola, L., Hartmann, W., Tholen, D., Brown, R., Matthews, C., and Bell, J. (1991). Solid c $\equiv$ n bearing material on outer solar system bodies. *Icarus 94*, pages 345–353.

Grundy, W., Bertrand, T., Binzel, R., Buie, M., Buratti, B., Cheng, A., Cook, J., Cruikshank, D., Devins, S., Dalle Ore, C., Earle, A., Ennico, K., Forget, F., Gao, P., Gladstone, G., Howett, C., Jennings, D., Kammer, J., Lauer, T., Linscott, I., Lisse, C., Lunsford, A., McKinnon, W., Olkin, C., Parker, A., Protopapa, S., Quirico, E., Reuter, D., Schmitt, B., Singer, K., Spencer, J., Stern, S., Strobel, D., Summers, M., Weaver, H., Weigle, G., Wong, M., Young, E., Young, L., and Zhang, X. (2018). Pluto's haze as a surface material. *Icarus 306*, pages 232–245.

Hapke, B. (1993). *Theory of Reflectance and Emittance Spectroscopy*. Cambridge University Press, Cambridge.

Hapke, B. (2002). Bidirectional reflectance spectroscopy: 5. the coherent backscatter opposition effect and anisotropic scattering. *Icarus 157*, pages 523–534.

Hapke, B. (2008). Bidirectional reflectance spectroscopy: 6. effects of porosity. *Icarus 198*, pages 918–926.

Hapke, B. (2012). Bidirectional reflectance spectroscopy: 7. tthe single particle phase function hockey stick relation. *Icarus 221*, pages 1079–1083.

Johnson, R., Carlson, R., Cooper, J., Paranicas, C., Moore, M., and Wong, M. (2004). Radiation effects on the surfaces of the galilean satellites. *Jupiter. The Planet, Satellites and Magnetosphere, Bagenal, F., Dowling, T.E., McKinnon, W.B.*, pages 485–512.

Khare, B., Sagan, C., Arakawa, E., Suits, F., Callcott, T., and Williams, M. (1984). Optical constants of organic tholins produced in a simulated titanian atmosphere: From soft x-ray to microwave frequencies. *Icarus 60*, pages 127–137.

Mahjoub, A., Carrasco, N., Dahoo, P.-R., Gautier, T., Szopa, C., and Cernogora, G. (2012). Influence of methane concentration on the optical indices of titan's aerosols analogues. *Icarus 221*, pages 670–677.

Poch, O., Pommerol, A., Jost, B., Carrasco, N., Szopa, C., and Thomas, N. (2016). Sublimation of ice-tholins mixtures: a morphological and spectrophotometric study. *Icarus 266*, pages 288–305.

Potin, S., Brissaud, O., Beck, P., Schmitt, B., Magnard, Y., Correia, J.-J., Rabou, P., and Jocou, L. (2018). Shadows: A spectro-gonio radiometer for bidirectional reflectance studies of dark meteorites and terrestrial analogues. design, calibrations and performances on challenging surfaces. *TBD*, page TBD.

Roush, T. and Dalton, J. (2004). Reflectance spectra of hydrated titan tholins at cryogenic temperatures and implications for compositional interpretation of red objects in the outer solar system. *Icarus 168*, pages 158–162.

Schmitt, B., Philippe, S., Grundy, W., Reuter, D., Cote, R., Quirico, E., Protopapa, S., Young, L., Binzel, R., Cook, J., Cruikshank, D., Dalle Ore, C., A.M., E., Ennico, K., Howett, C., Jennings, D., Linscott, I., Lunsford, A., Olkin, C., Parker, A., Parker, J., Singer, K., Spencer, J., Stansberry, J., Stern, S., Tsang, C., Verbiscer, A., Weaver, H., and the New Horizons Team (2017). Physical state and distribution of materials at the surface of pluto from new horizons leisa imaging spectrometer. *Icarus 287*, pages 229–260.

Sciamma-O'Brien, E., Dahoo, P.-R., Hadamcik, E., Carrasco, N., Quirico, E., Szopa, C., and Cernogora, G. (2012). Optical constants from 370 nm to 900 nm of titan tholins produced in a low pressure rf plasma discharge. *Icarus 218*, pages 356–363.

Workman, J. (1996). Interpretive spectroscopy for near infrared. *Applied Spectroscopy Reviews*, pages 251–320.

8 Appendices

8.1 Hapke's model formulae

The initial formulation of Hapke's reflectance model is provided in Hapke (1993) and updates of this model were found in Hapke (2002), Hapke (2008) and Hapke (2012).

The **Single Scattering Albedo** (corresponding to the ratio of the scattering efficiency to the total extinction efficiency) is expressed as follows:

$$w = Q_S/Q_E$$

$$\begin{aligned}
&\text{where } Q_E = 1 \\
&\qquad Q_S = S_e + (1 - S_e)\frac{1 - S_i}{1 - S_i\Theta}\Theta \\
&\text{with } S_e = \frac{(n-1)^2 + k^2}{(n+1)^2 + k^2} + 0.05 \\
&\qquad S_i = 1 - \frac{4}{n(n+1)^2} \\
&\qquad \Theta = e^{-\alpha < D >} \\
&\qquad < D >= \frac{2}{3}D \text{ and } D \text{ is the particles mean diameter}
\end{aligned} \tag{15}$$

where $< D >= \frac{2}{3}\left[n^2 - \frac{1}{n}\left(n^2 - 1\right)^{3/2}\right] D$ and D is the particles mean diameter

If the particle mean size is small enough so that the following condition is no longer matched $D \cdot \pi \geq \lambda$, then we have to switch to a different scattering regime, the so-called Rayleigh scattering. It leads to the modification of the single scattering albedo equations. Indeed, the single scattering albedo is given by Equation if we have $D \cdot \pi < \lambda$.

$$w = Q_S/Q_E$$

$$\begin{aligned}
\text{where } Q_E &= \frac{24nk}{(n^2+k^2)^2 + 4(n^2-k^2) + 4}\left(\frac{\pi D}{\lambda}\right) \\
Q_S &= \frac{8}{3}\frac{\left[(n^2+k^2)^2 + n^2 - k^2 - 2\right]^2 + 36n^2k^2}{\left[(n^2+k^2)^2 + 4(n^2-k^2) + 4\right]^2}\left(\frac{\pi D}{\lambda}\right)^4
\end{aligned} \tag{16}$$

Finally, the equations which give the single scattering albedo can also be modified if we want to account for the presence of internal scatterers (Hapke, 1993). If such internal scatterers are present, the single scattering albedo is still given by Equation 15 but the formula giving the internal-transmission factor Θ is modified as follows:

$$\begin{aligned}
\Theta =& \frac{r_i + \exp(-\sqrt{\alpha(\alpha+s)}\langle D\rangle))}{1 + r_i\exp(-\sqrt{\alpha(\alpha+s)}\langle D\rangle)} \\
&\text{where } r_i \text{ is given by: } r_i = \frac{1 - \sqrt{\alpha/(\alpha+s)}}{1 + \sqrt{\alpha/(\alpha+s)}} \\
&\text{and } s \text{ is the internal scattering coefficient.}
\end{aligned} \tag{17}$$

The definition of the **shadowing function** $S(i, e, g)$ accounting for the roughness of the surface and its impact on the reflectance is not straightforward and requires the definition of numerous intermediate functions.

$$\chi(\bar{\theta}) = \frac{1}{\sqrt{1 + \pi\tan^2(\bar{\theta})}} \tag{18}$$

$$E_1(x) = \exp\left(-\frac{2}{\pi\tan(\bar{\theta})\tan(x)}\right) \tag{19}$$

$$E_2(x) = \exp\left(-\frac{1}{\pi\tan^2(\bar{\theta})\tan^2(x)}\right) \tag{20}$$

$$f(g) = \exp\left(-2\tan(\frac{g}{2})\right) \tag{21}$$

$$\eta(y) = \chi(\bar{\theta})\left(\cos(y) + \sin(y)\tan(\bar{\theta})\frac{E_2(y)}{2 - E_1(y)}\right) \tag{22}$$

where x can either be the emergent or the incident angle.

Two different cases coexist, depending on the order between the emergent angle and the incident angle:

- If $e \geq i$

$$\mu_{0e} = \cos(i_e) = \chi(\bar{\theta}) \left(\cos(i) + \sin(i) \tan(\bar{\theta}) \frac{\cos(g) E_2(e) + \sin^2(g/2) E_2(i)}{2 - E_1(e) - (g/\pi) E_1(i)} \right) \tag{23}$$

$$\mu_e = \cos(e_e) = \chi(\bar{\theta}) \left(\cos(e) + \sin(e) \tan(\bar{\theta}) \frac{E_2(e) + \sin^2(g/2) E_2(i)}{2 - E_1(e) - (g/\pi) E_1(i)} \right) \tag{24}$$

$$S(i, e, g) = \frac{\mu_e}{\eta(e)} \frac{\mu_0}{\eta(i)} \frac{\chi(\bar{\theta})}{1 - f(g) + f(g) \chi(\bar{\theta}) \left(\mu_0 / \eta(i) \right)} \tag{25}$$

- If $e \leq i$

$$\mu_{0e} = \cos(i_e) = \chi(\bar{\theta}) \left(\cos(i) + \sin(i) \tan(\bar{\theta}) \frac{E_2(i) + \sin^2(g/2) E_2(e)}{2 - E_1(i) - (g/\pi) E_1(e)} \right) \tag{26}$$

$$\mu_e = \cos(e_e) = \chi(\bar{\theta}) \left(\cos(e) + \sin(e) \tan(\bar{\theta}) \frac{\cos(g) E_2(i) + \sin^2(g/2) E_2(e)}{2 - E_1(i) - (g/\pi) E_1(e)} \right) \tag{27}$$

$$S(i, e, g) = \frac{\mu_e}{\eta(e)} \frac{\mu_0}{\eta(i)} \frac{\chi(\bar{\theta})}{1 - f(g) + f(g) \chi(\bar{\theta}) \left(\mu_0 / \eta(e) \right)} \tag{28}$$

The **phase function** $P(g, \lambda)$ is usually modelled by well-known parametrised functions: the Henyey-Greenstein functions are the mostly used ones (Legendre functions might be used as well). The Henyey-Greenstein functions are divided into some groups, depending on the number of scattering lobes they present (1 or 2) and depending on their asymmetry parameters as well. Hapke advocates for using a two lobes Henyey-Greenstein function, which is more representative if the phase angle covers a large scale. The phase function he describes is given by the following expression:

$$P(g) = \frac{1 + c}{2} \frac{1 - b^2}{(1 - 2b \cos g + b^2)^{3/2}} + \frac{1 - c}{2} \frac{1 - b^2}{(1 + 2b \cos g + b^2)^{3/2}} \tag{29}$$

b is the width parameter and is constrained to be in the range $0 \leq b < 1$. There is no constraint on the parameter c except that the phase function has to be globally positive (so $P(g) \geq 0$). The first term of Equation 29 corresponds to the backscatter lobe whereas the second term describes the forward-scatter lobe. If c is positive, then the backscattering predominates and the other way around with the forward-scattering if c is negative. The larger the width parameter b is the narrower and higher the lobe is.

The **opposition effect** describes the brightness peak observed at very small phase angles (close to 0 deg). As explained in section 3.1. of this report, it is composed of two combined effects: *Shadow-Hiding Opposition Effect* (SHOE) and *Coherent Backscattering Opposition Effect* (CBOE). These two contributions are expressed with the following expressions. Starting with the SHOE contribution:

$$B_{\mathrm{SH}}(g) = 1 + B_{\mathrm{S0}} \cdot B_{\mathrm{S}}(g) \tag{30}$$

where B_{S0} is the amplitude of SHOE and with

$B_{\mathrm{S}}(g) = \left[1 + \frac{1}{h_{\mathrm{s}}} \tan\left(\frac{g}{2} \right) \right]^{-1}$ where h_{s} is the angular width of the shadow-hiding opposition effect

On the other hand, the Coherent-Backscattering Opposition Effect can be expressed with the following relations:

$$B_{\mathrm{CB}}(g) = 1 + B_{\mathrm{C0}} \cdot B_{\mathrm{C}}(g) \tag{31}$$

where B_{C0} is the amplitude of CBOE and

$B_{\mathrm{C}}(g) = \frac{1 + \frac{1 - \exp[-(1/h_{\mathrm{c}}) \tan(g/2)]}{(1/h_{\mathrm{c}}) \tan(g/2)}}{2 \left[1 + (1/h_{\mathrm{c}}) \tan(g/2) \right]^2}$ where h_{c} is the angular width of the coherent-backscattering opposition effect

8.2 Mixing formulae

Hapke's model also includes the possibility to account for different kind of mixtures. The equations which rule the different ways to mix materials are provided below.

8.2.1 Maxwell - Garnett effective medium model

Maxwell-Garnett model is useful when materials are mixed at spatial scale smaller than the wavelength. This model holds for mixtures where particles are suspended in an other material so that these particles and the distance between them are smaller than the wavelength. We will refer to the main material as medium 1 and to the particles as medium 2. The Maxwell-Garnett defines the effective dielectric constant of the medium from the dielectric constants ϵ_1 and ϵ_2 of the matrix (medium 1) and the inclusions (medium 2), respectively. Here, we are interested in the optical constants n and k which are related to the dielectric constant ϵ as follows: $\epsilon = (n + i \cdot k)^2$. If we note p the fraction of embedded material (medium 2) among the matrix (medium 1), the effective dielectric constant ϵ_{eff} is given by:

$$\epsilon_{\text{eff}} = \epsilon_1 + 3p\epsilon_1 \frac{\epsilon_2 - \epsilon_1}{\epsilon_2 + 2\epsilon_1 - p(\epsilon_2 - \epsilon_1)} \tag{32}$$

Once the effective dielectric constant has been determined, we can deduce the corresponding optical constants n_{eff} and k_{eff}:

$$\begin{aligned} n_{\text{eff}} &= \text{real}(\epsilon_{\text{eff}}) \\ k_{\text{eff}} &= \text{imaginary}(\epsilon_{\text{eff}}) \end{aligned} \tag{33}$$

The optical constants of the effective medium can then be used in any model we like.

8.2.2 Spatial mixing

Spatial mixing (also called areal mixing) corresponds to a non-homogeneous mixing in which the surface is composed of several unmixed parts made of one single material. These parts are lying next to each other and form the global mixing. The resulting mixture is non-homogeneous because the mixing does not occur at the particles scale. Spatial mixing is simply modelled with a linear model: the contribution of one material to the total reflectance of the mixture is the reflectance of this particular material weighted by the area fraction it covers.

$$\text{REFF}_{\text{mixture}} = \sum_i f_i \cdot \text{REFF}_{\text{material } i} \tag{34}$$

where f_i corresponds to the fraction of the total mixture area covered by the i^{th} material

8.2.3 Intimate mixing

Intimate mixtures are homogeneous mixtures in which several materials are mixed at the individual particle scale. To model such mixtures, a simple linear combination of the different contributing materials does not work (contrarily to spatial mixing). We need to calculate the averaged scattering albedo, phase function and opposition effect terms to be able to determine the resulting reflectance. The formulae which give these averaged variables are provided below.

The averaged single scattering albedo is given by the following formula:

$$w = \frac{\sum_j \frac{m_j Q_{Sj}}{\rho_j D_j}}{\sum_j \frac{m_j Q_{Ej}}{\rho_j D_j}} \tag{35}$$

where m_j is the mass fraction of the j^{th} material

ρ_j is the solid density of the j^{th} material

D_j is the particle diameter of the j^{th} material

As stated in Equation 15, the single scattering albedo of a given material is defined by:

$$w = Q_S / Q_E \tag{36}$$

As $Q_E = 1$ and $w = Q_S/Q_E$, the averaged single scattering albedo can be expressed as follows:

$$w = \left(\sum_j \frac{m_j w_j}{\rho_j D_j} \right) / \left(\sum_j \frac{m_j}{\rho_j D_j} \right) \tag{37}$$

where w_j is the single scattering albedo of the j^{th} material

For the phase function, the averaged value for P follows from the equation below.

$$P = \frac{\sum_j \frac{m_j Q_{Sj} P_j}{\rho_j D_j}}{\sum_j \frac{m_j Q_{Sj}}{\rho_j D_j}} \tag{38}$$

$$\Rightarrow \; P = \left(\frac{m_j w_j P_j}{\rho_j D_j}\right) / \left(\frac{m_j w_j}{\rho_j D_j}\right) \tag{39}$$

where P_j is the phase function of the j^{th} material

The shadow-hiding opposition effect terms are also impacted by the way particles are mixed together in an intimate mixture. The averaged shadow-hiding opposition effect coefficient B_{S0} is defined by:

$$B_{\text{S0}}(\lambda) = \frac{\sum_j \frac{m_j Q_{Ej} S_j(0)}{\rho_j D_j}}{\sum_j \frac{m_j Q_{Ej} w_j(\lambda) P_j(0)}{\rho_j D_j}} \tag{40}$$

$$\Rightarrow B_{\text{S0}}(\lambda) = \left(\sum_j \frac{m_j S_j(0)}{\rho_j D_j}\right) / \left(\frac{m_j w_j(\lambda) P_j(0)}{\rho_j D_j}\right) \tag{41}$$

because the shadow-hiding opposition effect coefficient is given by: $B_{S0} = \dfrac{S(0)}{w(\lambda) \cdot P(0)}$

From these averaged variables, we can calculate the averaged reflectance by plugging in them into Equation 6.

8.3 Inversion of Hapke's model

As exposed in section 3.4.1 of this report, Hapke's model has been simplified for inversion purposes. As a reminder, we have decided to neglect the porosity effects, as well as the shadowing function and the opposition effect. We also have assumed that the phase function does not depend on the wavelength and is therefore a function of the phase angle g only. We have ended up with the following expression for the reflectance $r(i, e, g, \lambda)$:

$$r(i, e, g, \lambda) = \frac{\omega(\lambda)}{4\pi} \frac{\mu_0}{\mu_0 + \mu} \left[P(g) + H(w, \mu_0)H(w, \mu) - 1\right] \tag{42}$$

What we have measured is not exactly the reflectance but rather the reflectance factor REFF defined as $\text{REFF} = \frac{r(i,e,g,\lambda)\cdot\pi}{\mu_0}$ so the formula we are interested in is:

$$\text{REFF}(i, e, g, \lambda) = \frac{\omega(\lambda)}{4} \frac{1}{\mu_0 + \mu} \left[P(g) + H(w, \mu_0)H(w, \mu) - 1\right] \tag{43}$$

We want to determine the single scattering albedo w and the phase function P. To this end, we have access to 42 spectra for each tholins sample. Indeed, we have measured spectra at 14 different emergent angles and this has been conducted for 3 different incident angles. 105 wavelengths are available for each spectrum and we have performed measurements for 13 different phase angles (from $g = 10$ deg to $g = 130$ deg with steps of 10 deg). Therefore, we end up with 118 unknowns: 105 unknowns correspond to the values of w for each wavelength and the remaining 13 unknowns correspond to the values of the phase function P for each phase angle g.

Let us note X the vector containing all the unknowns and defined as:

$$X = \begin{pmatrix} w(\lambda_1) \\ w(\lambda_2) \\ ... \\ ... \\ w(\lambda_{105}) \\ P(g = 10 \text{ deg}) \\ P(g = 20 \text{ deg}) \\ ... \\ ... \\ P(g = 130 \text{ deg}) \end{pmatrix} \tag{44}$$

The measurements are contained in the vector Y and organised as follows: the vector Y is built as the combination of the 42 spectra. It contains the reflectance values for the 105 wavelengths of one spectrum, followed by the 105 reflectance values of the next spectrum. Finally, we end up with 42 spectra composed of 105 values, each spectrum following the previous one (so 4410 measurement values in total).

$$Y = \begin{pmatrix} \text{REFF}(i_1, e_1, g_1, \lambda_1) \\ \text{REFF}(i_1, e_1, g_1, \lambda_2) \\ \text{REFF}(i_1, e_1, g_1, \lambda_3) \\ ... \\ \text{REFF}(i_1, e_1, g_1, \lambda_{105}) \\ \text{REFF}(i_2, e_2, g_2, \lambda_1) \\ \text{REFF}(i_2, e_2, g_2, \lambda_2) \\ ... \\ ... \\ \text{REFF}(i_{42}, e_{42}, g_{42}, \lambda_{105}) \end{pmatrix} \tag{45}$$

As Hapke's model is highly non-linear, the measurements value are linked to the unknowns vector via a function that we will call A as $Y = A(X)$. This function corresponds of course to Hapke's model (see Equation 43) and depends on the geometry angles (incidence, emergence and phase angles). A is actually a matrix function and is defined by the following expression (directly

deduced from the formulation of the simplified Hapke's model (Equation 43)).

$$
\begin{aligned}
A(X) &= \begin{pmatrix}
\text{REFF}(i_1, e_1, g_1, \lambda_1) \\
\text{REFF}(i_1, e_1, g_1, \lambda_2) \\
... \\
\text{REFF}(i_1, e_1, g_1, \lambda_{105}) \\
\text{REFF}(i_2, e_2, g_2, \lambda_1) \\
\text{REFF}(i_2, e_2, g_2, \lambda_2) \\
... \\
... \\
\text{REFF}(i_{42}, e_{42}, g_{42}, \lambda_{105})
\end{pmatrix} \\
&= \begin{pmatrix}
\frac{\omega(\lambda_1)}{4} \frac{1}{\cos(i_1)+\cos(e_1)} \left[P(g_1) + H(w(\lambda_1), \cos(i_1))H(w(\lambda_1), \cos(e_1)) - 1\right] \\
\frac{\omega(\lambda_2)}{4} \frac{1}{\cos(i_1)+\cos(e_1)} \left[P(g_1) + H(w(\lambda_2), \cos(i_1))H(w(\lambda_2), \cos(e_1)) - 1\right] \\
..... \\
\frac{\omega(\lambda_{105})}{4} \frac{1}{\cos(i_1)+\cos(e_1)} \left[P(g_1) + H(w(\lambda_{105}), \cos(i_1))H(w(\lambda_{105}), \cos(e_1)) - 1\right] \\
\frac{\omega(\lambda_1)}{4} \frac{1}{\cos(i_2)+\cos(e_2)} \left[P(g_2) + H(w(\lambda_1), \cos(i_2))H(w(\lambda_1), \cos(e_2)) - 1\right] \\
\frac{\omega(\lambda_2)}{4} \frac{1}{\cos(i_2)+\cos(e_2)} \left[P(g_2) + H(w(\lambda_2), \cos(i_2))H(w(\lambda_2), \cos(e_2)) - 1\right] \\
..... \\
..... \\
\frac{\omega(\lambda_{105})}{4} \frac{1}{\cos(i_{42})+\cos(e_{42})} \left[P(g_{42}) + H(w(\lambda_{105}), \cos(i_{42}))H(w(\lambda_{105}), \cos(e_{42})) - 1\right]
\end{pmatrix}
\end{aligned}
\tag{46}
$$

Knowing the corresponding geometry angles (incidence, emergence and phase angles) for each of the 42 spectra, A gives the reflectance as a function of the unknowns vector only. As already stated, this problem is non-linear and cannot be directly inverted. To invert it, we need to linearise the main equation $Y = A(X)$ around the point X_0. To this end, we will write the first term of the Taylor series of this equation:

$$
Y = A(X_0) + \left.\frac{\partial A(X)}{\partial X}\right|_0 (X - X_0) \text{ where we have by definition } A(X_0) = Y_0 \tag{47}
$$

$$
\Rightarrow \Delta Y = \frac{\partial A(X_0)}{\partial X_0} \Delta X \text{ where we define: } \Delta Y = Y - Y_0 \text{ and } \Delta X = X - X_0 \tag{48}
$$

Replacing the function A by the function The non-linear least squares is therefore an iterative process: we have brought us back to a linearised system. At each iteration, we can derive the value of ΔX that we should apply to the current unknown vector X to update it. After this update, the value $X_0 + \Delta X$ becomes the new X_0. From this new value of X_0, we calculate the corresponding value of Y_0 using $Y_0 = A(X_0)$. We keep iterating until the system reaches convergence (the convergence is reached when the ΔX values become small enough to be inferior to the convergence limit).

In order to implement such a method, we need to more precisely define the system $\Delta Y = \frac{\partial A(X)}{\partial X} \Delta X$ and especially the formulation of $\frac{\partial A(X)}{\partial X}$. For each spectrum, we know the value of the corresponding phase angle g. The repartition of the 42 spectra has been conducted as follows (of course each spectrum is made of 105 values (105 different wavelengths)):

$$Y = \begin{pmatrix} 1^{\text{st}} \text{ spectrum: } i_1 = 0,\ e_1 = -10,\ g_1 = 10 \\ 2^{\text{nd}} \text{ spectrum: } i_2 = 0,\ e_2 = -20,\ g_2 = 20 \\ 3^{\text{rd}} \text{ spectrum: } i_3 = 0,\ e_3 = -30,\ g_3 = 30 \\ 4^{\text{th}} \text{ spectrum: } i_4 = 0,\ e_4 = -40,\ g_4 = 40 \\ 5^{\text{th}} \text{ spectrum: } i_5 = 0,\ e_5 = -50,\ g_5 = 50 \\ 6^{\text{th}} \text{ spectrum: } i_6 = 0,\ e_6 = -60,\ g_6 = 60 \\ 7^{\text{th}} \text{ spectrum: } i_7 = 0,\ e_7 = -70,\ g_7 = 70 \\ 8^{\text{th}} \text{ spectrum: } i_8 = 0,\ e_8 = 10,\ g_8 = 10 \\ 9^{\text{th}} \text{ spectrum: } i_9 = 0,\ e_9 = 20,\ g_9 = 20 \\ 10^{\text{th}} \text{ spectrum: } i_{10} = 0,\ e_{10} = 30,\ g_{10} = 30 \\ 11^{\text{th}} \text{ spectrum: } i_{11} = 0,\ e_{11} = 40,\ g_{11} = 40 \\ 12^{\text{th}} \text{ spectrum: } i_{12} = 0,\ e_{12} = 50,\ g_{12} = 50 \\ 13^{\text{th}} \text{ spectrum: } i_{13} = 0,\ e_{13} = 60,\ g_{13} = 60 \\ 14^{\text{th}} \text{ spectrum: } i_{14} = 0,\ e_{14} = 70,\ g_{14} = 70 \\ 15^{\text{th}} \text{ spectrum: } i_{15} = 30,\ e_{15} = -10,\ g_{15} = 40 \\ 16^{\text{th}} \text{ spectrum: } i_{16} = 30,\ e_{16} = -20,\ g_{16} = 50 \\ 17^{\text{th}} \text{ spectrum: } i_{17} = 30,\ e_{17} = -30,\ g_{17} = 60 \\ 18^{\text{th}} \text{ spectrum: } i_{18} = 30,\ e_{18} = -40,\ g_{18} = 70 \\ 19^{\text{th}} \text{ spectrum: } i_{19} = 30,\ e_{19} = -50,\ g_{19} = 80 \\ 20^{\text{th}} \text{ spectrum: } i_{20} = 30,\ e_{20} = -60,\ g_{20} = 90 \\ 21^{\text{st}} \text{ spectrum: } i_{21} = 30,\ e_{21} = -70,\ g_{21} = 100 \\ 22^{\text{nd}} \text{ spectrum: } i_{22} = 30,\ e_{22} = 10,\ g_{22} = 20 \\ 23^{\text{rd}} \text{ spectrum: } i_{23} = 30,\ e_{23} = 20,\ g_{23} = 10 \\ 24^{\text{th}} \text{ spectrum: } i_{24} = 30,\ e_{24} = 0,\ g_{24} = 30 \\ 25^{\text{th}} \text{ spectrum: } i_{25} = 30,\ e_{25} = 40,\ g_{25} = 10 \\ 26^{\text{th}} \text{ spectrum: } i_{26} = 30,\ e_{26} = 50,\ g_{26} = 20 \\ 27^{\text{th}} \text{ spectrum: } i_{27} = 30,\ e_{27} = 60,\ g_{27} = 30 \\ 28^{\text{th}} \text{ spectrum: } i_{28} = 30,\ e_{28} = 70,\ g_{28} = 40 \\ 29^{\text{th}} \text{ spectrum: } i_{29} = 60,\ e_{29} = -10,\ g_{29} = 70 \\ 30^{\text{th}} \text{ spectrum: } i_{30} = 60,\ e_{30} = -20,\ g_{30} = 80 \\ 31^{\text{st}} \text{ spectrum: } i_{31} = 60,\ e_{31} = -30,\ g_{31} = 90 \\ 32^{\text{nd}} \text{ spectrum: } i_{32} = 60,\ e_{32} = -40,\ g_{32} = 100 \\ 33^{\text{rd}} \text{ spectrum: } i_{33} = 60,\ e_{33} = -50,\ g_{33} = 110 \\ 34^{\text{th}} \text{ spectrum: } i_{34} = 60,\ e_{34} = -60,\ g_{34} = 120 \\ 35^{\text{th}} \text{ spectrum: } i_{35} = 60,\ e_{35} = -70,\ g_{35} = 130 \\ 36^{\text{th}} \text{ spectrum: } i_{36} = 60,\ e_{36} = 10,\ g_{36} = 50 \\ 37^{\text{th}} \text{ spectrum: } i_{37} = 60,\ e_{37} = 20,\ g_{37} = 40 \\ 38^{\text{th}} \text{ spectrum: } i_{38} = 60,\ e_{38} = 30,\ g_{38} = 30 \\ 39^{\text{th}} \text{ spectrum: } i_{39} = 60,\ e_{39} = 40,\ g_{39} = 20 \\ 40^{\text{th}} \text{ spectrum: } i_{40} = 60,\ e_{40} = 50,\ g_{40} = 10 \\ 41^{\text{st}} \text{ spectrum: } i_{41} = 60,\ e_{41} = 0,\ g_{41} = 60 \\ 42^{\text{nd}} \text{ spectrum: } i_{42} = 60,\ e_{42} = 70,\ g_{42} = 10 \end{pmatrix} \tag{49}$$

Looking at the way the measurements values are organised in the vector Y, the matrix $\frac{\partial A(X)}{\partial X}$ will have the following shape:

$$\Delta Y = \frac{\partial A(X)}{\partial X}\Delta X = \frac{\partial A(X)}{\partial X} \cdot \begin{pmatrix} \Delta w(\lambda_1) \\ \Delta w(\lambda_2) \\ \Delta w(\lambda_3) \\ \dots \\ \dots \\ \Delta w(\lambda_{105}) \\ \Delta P(g=10) \\ \Delta P(g=20) \\ \dots \\ \dots \\ \Delta P(g=130) \end{pmatrix}$$

$$= \begin{pmatrix} \frac{\partial \text{REFF}(i_1,e_1,g_1,\lambda_1)}{\partial w(\lambda_1)} & 0 & \dots & \dots & 0 & \frac{\partial \text{REFF}(i_1,e_1,g_1,\lambda_1)}{\partial P(g_1=10)} & 0 & \dots & 0 \\ 0 & \frac{\partial \text{REFF}(i_1,e_1,g_1,\lambda_2)}{\partial w(\lambda_2)} & \dots & \dots & 0 & \frac{\partial \text{REFF}(i_1,e_1,g_1,\lambda_2)}{\partial P(g_1=10)} & 0 & \dots & 0 \\ 0 & 0 & \dots & \dots & 0 & \frac{\partial \text{REFF}(i_1,e_1,g_1,\lambda_3)}{\partial P(g_1=10)} & 0 & \dots & 0 \\ \dots & \dots & \dots & \dots & \dots & \dots & \dots & \dots & \dots \\ \dots & \dots & \dots & \dots & 0 & \frac{\partial \text{REFF}(i_1,e_1,g_1,\lambda_{104})}{\partial P(g_1=10)} & 0 & \dots & 0 \\ 0 & 0 & \dots & 0 & \frac{\partial \text{REFF}(i_1,e_1,g_1,\lambda_{105})}{\partial w(\lambda_{105})} & \frac{\partial \text{REFF}(i_1,e_1,g_1,\lambda_{105})}{\partial P(g_1=10)} & 0 & \dots & 0 \\ \frac{\partial \text{REFF}(i_2,e_2,g_2,\lambda_1)}{\partial w(\lambda_1)} & 0 & \dots & \dots & 0 & 0 & \frac{\partial \text{REFF}(i_2,e_2,g_2,\lambda_1)}{\partial P(g_2=20)} & \dots & 0 \\ 0 & \frac{\partial \text{REFF}(i_2,e_2,g_2\lambda_2)}{\partial w(\lambda_2)} & \dots & \dots & 0 & 0 & \frac{\partial \text{REFF}(i_2,e_2,g_2,\lambda_2)}{\partial P(g_2=20)} & \dots & 0 \\ 0 & 0 & \dots & \dots & 0 & 0 & \frac{\partial \text{REFF}(i_2,e_2,g_2,\lambda_3)}{\partial P(g_2=20)} & \dots & 0 \\ \dots & \dots & \dots & \dots & \dots & \dots & \dots & \dots & \dots \\ \dots & \dots & \dots & \dots & 0 & 0 & \frac{\partial \text{REFF}(i_2,e_2,g_2,\lambda_{104})}{\partial P(g_2=20)} & \dots & 0 \\ 0 & 0 & \dots & 0 & \frac{\partial \text{REFF}(i_2,e_2,g_2,\lambda_{105})}{\partial w(\lambda_{105})} & 0 & \frac{\partial \text{REFF}(i_2,e_2,g_2,\lambda 105)}{\partial P(g_2=20)} & \dots & 0 \\ \dots & \dots & \dots & \dots & \dots & \dots & \dots & \dots & \dots \\ \dots & \dots & \dots & \dots & \dots & \dots & \dots & \dots & \dots \\ \dots & \dots & \dots & \dots & \dots & \dots & \dots & \dots & \dots \\ \frac{\partial \text{REFF}(i_{42},e_{42},g_{42},\lambda_1)}{\partial w(\lambda_1)} & 0 & \dots & \dots & 0 & \frac{\partial \text{REFF}(i_{42},e_{42},g_{42},\lambda_1)}{\partial P(g_{42}=10)} & 0 & \dots & 0 \\ 0 & \frac{\partial \text{REFF}(i_{42},e_{42},g_{42},\lambda_2)}{\partial w(\lambda_2)} & \dots & \dots & 0 & \frac{\partial \text{REFF}(i_{42},e_{42},g_{42},\lambda_2)}{\partial P(g_{42}=10)} & 0 & \dots & 0 \\ 0 & 0 & \dots & \dots & 0 & \frac{\partial \text{REFF}(i_{42},e_{42},g_{42},\lambda_3)}{\partial P(g_{42}=10)} & 0 & \dots & 0 \\ \dots & \dots & \dots & \dots & \dots & \dots & \dots & \dots & \dots \\ \dots & \dots & \dots & \dots & 0 & \frac{\partial \text{REFF}(i_{42},e_{42},g_{42},\lambda_{104})}{\partial P(g_{42}=10)} & 0 & \dots & 0 \\ 0 & 0 & \dots & 0 & \frac{\partial \text{REFF}(i_{42},e_{42},g_{42},\lambda_{105})}{\partial w(\lambda_{105})} & \frac{\partial \text{REFF}(i_{42},e_{42},g_{42},\lambda_{105})}{\partial P(g_{42}=10)} & 0 & \dots & 0 \end{pmatrix}$$

$$\cdot \begin{pmatrix} \Delta w(\lambda_1) \\ \Delta w(\lambda_2) \\ \Delta w(\lambda_3) \\ \dots \\ \dots \\ \Delta w(\lambda_{105}) \\ \Delta P(g=10) \\ \Delta P(g=20) \\ \dots \\ \dots \\ \Delta P(g=130) \end{pmatrix} \tag{50}$$

Now that we have built the matrix $\frac{\partial A(X)}{\partial X}$, we need to derive expressions for the two functions $\frac{\partial \text{REFF}}{\partial w}$ and $\frac{\partial \text{REFF}}{\partial P}$ which are involved in the definition of the matrix $\frac{\partial A(X)}{\partial X}$.

Starting from the simplified formulation of the reflectance factor REFF (see Equation 43)

$$\text{REFF}(i,e,g,\lambda) = \frac{\omega(\lambda)}{4}\frac{1}{\mu_0+\mu}\left[P(g) + H(w,\mu_0)H(w,\mu) - 1\right] \tag{51}$$

Let us define $\alpha(w,\mu_0,\mu)$ as:

$$\alpha = H(w,\mu_0)H_(w,\mu) \tag{52}$$

Using the simplified form for the Chandrasekhar function H:

$$\alpha(w,\mu_0,\mu) = H(w,\mu_0)H(w,\mu) = \frac{1+2\mu_0}{1+2\mu_0\sqrt{1-w}} \cdot \frac{1+2\mu}{1+2\mu\sqrt{1-w}} \tag{53}$$

Deriving REFF with respect to the single scattering albedo w:

$$\begin{aligned} \frac{\partial \text{REFF}}{\partial w} &= \frac{\partial}{\partial w}\left(\frac{w}{4}\frac{1}{\mu_0+\mu}\left[P+\alpha(w)-1\right]\right) \\ &= \frac{P+\alpha(w)-1}{4(\mu_0+\mu)} + \frac{w}{4(\mu_0+\mu)}\frac{\partial \alpha(w)}{\partial w} = \frac{1}{4(\mu_0+\mu)}\left[P-1+\alpha(w)+w\frac{\partial \alpha(w)}{\partial w}\right] \end{aligned} \tag{54}$$

$$\begin{aligned} \text{where:}\quad \frac{\partial \alpha(w)}{\partial w} &= \frac{\partial}{\partial w}\left(\frac{(1+2\mu_0)(1+2\mu)}{1+2(\mu_0+\mu)\sqrt{1-w}+4\mu_0\mu(1-w)}\right) \\ &= (1+2\mu_0)(1+2\mu)\left[\frac{\frac{(\mu_0+\mu)}{\sqrt{1-w}}+4\mu_0\mu}{\left(1+2(\mu_0+\mu)\sqrt{1-w}+4\mu_0\mu(1-w)\right)^2}\right] \end{aligned} \tag{55}$$

Now that we have an expression for the derivative of the reflectance factor with respect to w, we need an expression for the derivative of REFF with respect to the phase function P. This derivative is far more straightforward than the previous one.

$$\frac{\partial \text{REFF}}{\partial P} = \frac{w}{4} \frac{1}{\mu_0 + \mu} \tag{56}$$

Now that the matrix $\frac{\partial A(X)}{\partial X}$ is entirely defined, we can briefly detail the implementation of the non-linear least squares:

- Initialisation of the unknowns vector X: $X =$ outcome of the Monte-Carlo simulation
- Initialisation of the linearisation point: $X = X_0$
- Calculation of the system matrix at the point of linearisation $\left.\frac{\partial A(X)}{\partial X}\right|_0 = \frac{\partial A(X_0)}{\partial X_0}$
- Definition of the observation vector $\Delta Y = Y - Y_0 = Y - A(X_0)$ where Y is defined by Equation 49 and A by Equation 46
- Least-squares method applied to the linearised system defined by: $\Delta Y = \left.\frac{\partial A(X)}{\partial X}\right|_0 \Delta X$

  $\Delta X = \left[\left(\left.\frac{\partial A(X)}{\partial X}\right|_0 \right)^{\mathrm{T}} \left(\left.\frac{\partial A(X)}{\partial X}\right|_0 \right) \right]^{-1} \left(\left.\frac{\partial A(X)}{\partial X}\right|_0 \right)^{\mathrm{T}} \Delta Y$
- Update of the unknowns vector: $X_{\text{new}} = X_0 + \Delta X$
- Update of the linearisation point: $X_0 = X_{\text{new}}$
- Update of the observation vector : $\Delta Y = Y - A(X_{\text{new}})$
- We can then applied these new ΔY and also the system matrix $\frac{\partial A(X)}{\partial X}$ linearised around the new linearisation point to perform a second least-squares inversion and get a new update for the unknowns vector, and so on...
- So we keep iterating until we reach convergence

In order to assess the quality of the model inversion, we have plotted in Figure 24 the actual laboratory data we have measured (blue curves) as well as the associated reflectance calculated with Hapke's model, using the single scattering albedo and phase function resulting from the inversion (orange curves). The difference between the two curves have given us an estimation of the precision of this inversion method. For the sake of clarity, we will not provide a plot for each of the 42 geometry configurations under which we have measured spectra. 6 of these plots will be provided, with various phase angles to be more representative of the different configurations.

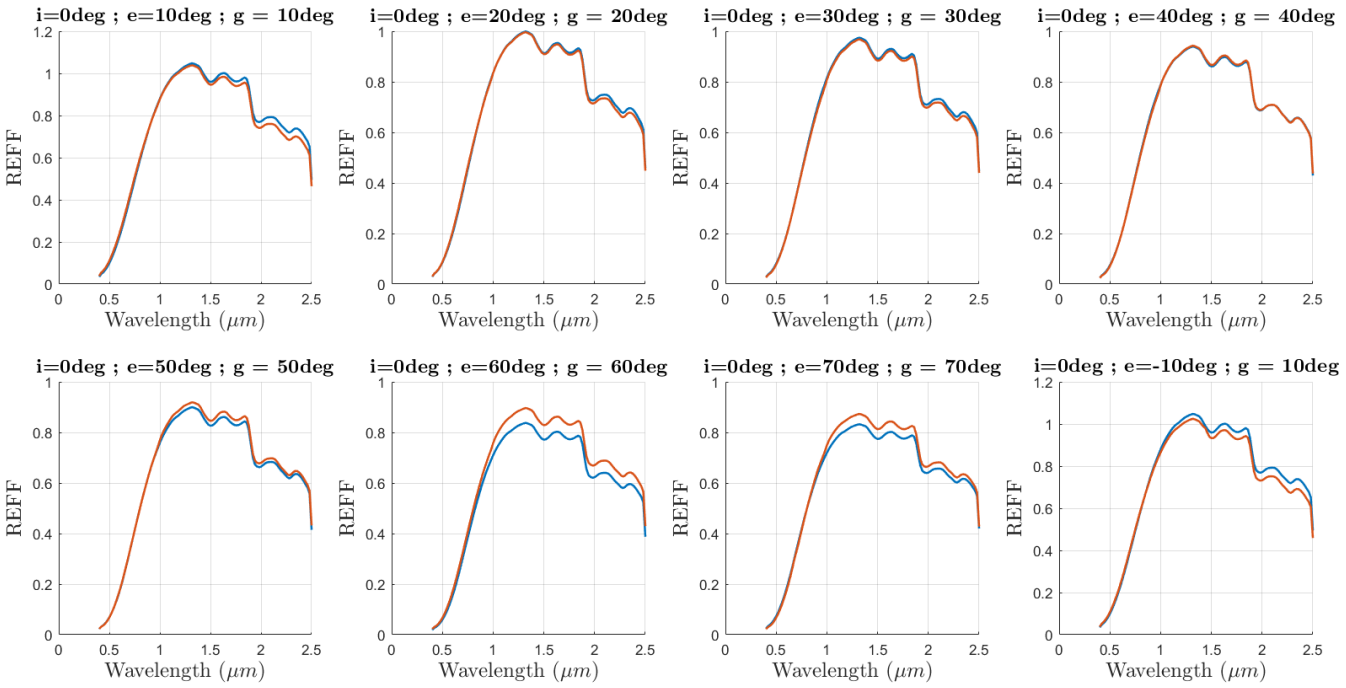

Figure 24: Results of the inversion of Hapke's model and comparison with laboratory data

We have observed that the quality of the inverted model decreases with increasing phase angles. There is apparently some effects which are not well reproduced , either because of some assumptions in the inversion technique or possibly because Hapke's model does not account for the entire complexity of the reflectance. Nonetheless and despite the small discrepancies we have observed, the inversion provides good results overall. The error is always smaller than 5%, which is perfectly acceptable regarding the simplifying assumptions we made and the complexity of the inversion process.

We have now obtained a pretty good estimation of the single scattering albedo by numerically inverting Hapke model. However, we may want to retrieve the optical constants n and k instead of the single scattering albedo ω. This is especially the case when we want to analyse the effect of the grain size on the reflectance of a surface (since the particles mean diameter only appears in the calculation of the single scattering albedo which also depends on n, k and the wavelength λ). Calculating the single scattering albedo from the optical constants n and k of a material while being able to vary the mean diameter D can be of interest. Moreover, retrieving the optical constants is a required step if we want to use effective medium theory (this is useful when we want to model icy grains condensed around a core material which could be tholins in our particular case).

In order to retrieve n and k from the inverted single scattering albedo, we have used the following method:

- We have first assumed the real part n of the refractive index is constant over our spectral range of interest. This is a relatively fair assumption regarding the optical constants available for tholins in the literature. We have parsed different values for n, going from 1 to 2 with a step of 0.05 (so 21 values in total). For each of these n values, we have derived the corresponding values for k with the method exposed below (k is not assumed to be constant so we have different values for k depending on the wavelength). Then, for each value of n, we have computed the total sum of squares between the inverted single scattering albedo and the single scattering albedo we calculated from our derived optical constants. We have finally selected the value of n which corresponds to the lowest total sum of squares (meaning the value of n from which we can best reproduce our targeted single scattering albedo).
- For a given value of n, we have derived the corresponding value for k using an iterative process based on the relation between n, k, λ and ω. Indeed, the single scattering albedo is expressed as follows (see Equation 15):

$$\omega(n,k,D,\lambda) = S_e + (1-S_e)\frac{1-S_i}{1-S_i\Theta}\Theta \tag{57}$$

where S_i is entirely determined by the value of n while S_e depends on the value of k we want to eventually determine.

So we have:

$$(1-S_i\Theta)(\omega - S_e) = (1-S_e)(1-S_i)\Theta \tag{58}$$

$$\Theta\left(S_i\omega + 1 - S_e - S_i\right) = \omega - S_e \tag{59}$$

$$\Rightarrow \Theta = \frac{w - S_e}{1 - S_e - S_i + S_i\omega} \tag{60}$$

Θ is related to the value of k by the following equation:

$$\Theta = \exp(-\alpha\langle D\rangle) \tag{61}$$

Considering the definition of the absorption coefficient $\alpha = (4\pi k)/\lambda$, a relation can be established between k and the following set of parameters: S_i, S_e, λ, $\langle D\rangle$ and ω:

$$\alpha = \frac{4\pi k}{\lambda} = -\frac{1}{\langle D\rangle}\ln\left(\frac{\omega - S_e}{1 - S_e - S_i + S_i\omega}\right) \tag{62}$$

$$\Rightarrow k = -\frac{\lambda}{4\pi\langle D\rangle}\ln\left(\frac{\omega - S_e}{1 - S_e - S_i + S_i\omega}\right) \tag{63}$$

However, we can note S_e is present on the right-hand side of Equation 63 while it depends on the value of k (see Equation 15). This is why we need an iterative process here: we first initialise the value of k (the initialising value for k has been chosen equal to 1e-4) then we plug this value in S_e and we update the value of k using Equation 63. Indeed, all the other variables in Equation 63 are fully defined (ω refers to the single scattering albedo from which we want to retrieve the optical constants). We keep iterating until our estimation of k reaches convergence (the convergence threshold being set to $10^(-12)$ here) and we conduct this iterative process for each wavelength as k is wavelength-dependent.

As explained before, we do this for different values of n. Once we have completed all the calculations, we are left with one set of k wavelength-dependent values for each value of n that has been considered. We finally select the set of k and n which best reproduces the single scattering albedo we are working on.

The results we have obtained with such an iterative method are pretty good: we have found n and k values that can very well reproduce the single scattering albedo from which they are extracted. Below are provided the results we have obtained for the

two types of pure tholins we have been working one (one with 5% of methane and the other one with 1% of methane only). We see that the differences between the single scattering albedo calculated from our estimated values of n and k and the inverted single scattering albedo they have been derived from are extremely low. We can therefore conclude our iterative algorithm is working well and provide reasonably trustworthy estimations of the optical constants.

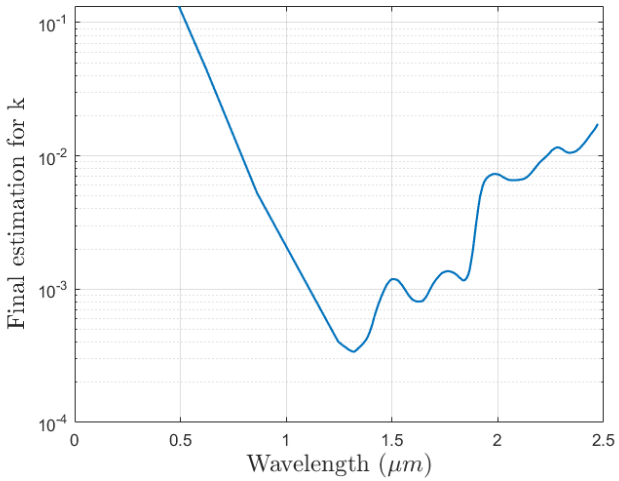

(a) k values for 95:5 tholins (the corresponding n is $n = 1.4$)

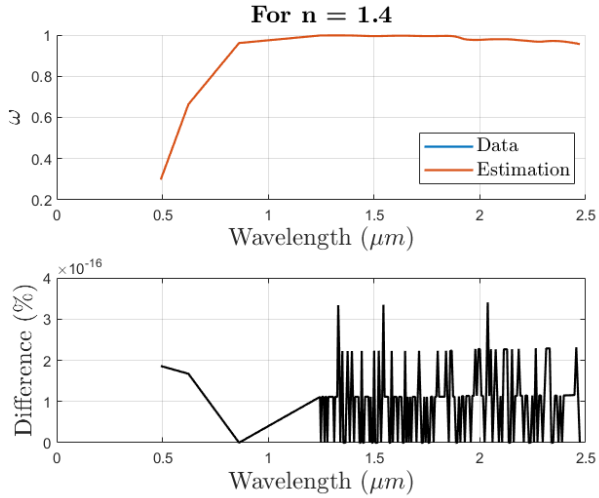

(b) Errors while trying to reproduce the single scattering albedo from the retrieved optical constants

Figure 25: Determination of n and k for pure tholins with 95% N_2, 5% CH_4

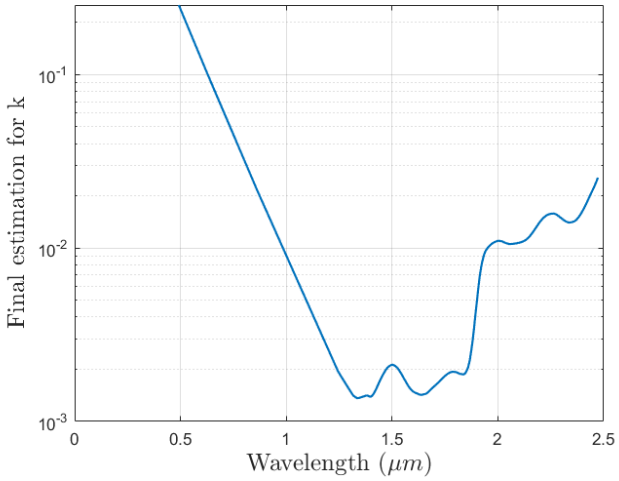

(a) k values for 99:1 tholins (the corresponding n is $n = 1.35$)

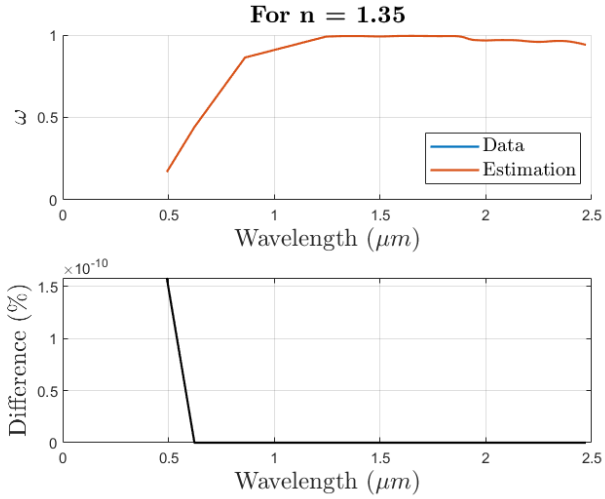

(b) Errors while trying to reproduce the single scattering albedo from the retrieved optical constants

Figure 26: Determination of n and k for pure tholins with 99% N_2, 1% CH_4

8.4 Correction for the geometry difference (tholins darkening)

The reflectance spectra of the darkened tholins have been measured under a standard geometry (i = 0 deg, e = 30 deg, Ψ = 0 deg) and we therefore need to correct them to compare with the New Horizons data (obtained under a different geometry). LEISA's illumination and observation geometry is defined as: i = 55 deg, e = 43.9 deg and g = 21.8 deg whereas our measurements were performed with i = 0 deg, e = 30 deg and g = 0 deg. However, the way to correct such a difference is not straightforward. Below are presented the main methods that had been considered to achieve this result. We should note here that each corrective method that has been tested is based on Hapke's reflectance model and therefore relies on the assumption that this model perfectly represents the reflectance of a surface, which of course it does not. The model does not account for the whole complexity of the actual reflectance behaviour of a surface but it is the best tool we could possibly use to derive such a geometry correction. Still it is worth keeping this in mind while considering the validity of the following corrective approaches.

– The geometry of New Horizons observation is relatively close to the following configuration (i = 60 deg, e = 40 deg and g = 20 deg (Ψ = 0 deg)) for which we do have measurements. This configuration is especially a good equivalent for that of the New Horizons data because the value of the azimuth angle Ψ (which is the only angle fundamentally different with respect to the New Horizons geometry) has no influence in our Hapke's model. Indeed, it only has an impact on the shadowing function, which has no effect if the macroscopic rugosity parameter is set to 0 deg (as it is the case here). If we now write the Hapke formula which determine the reflectance for both the standard geometry (i = 0 deg, e = 30 deg and Ψ = 0 deg) and the new geometry of interest (i = 60 deg, e = 40 deg and Ψ = 0 deg), which is the closest we have from that of the LEISA data:

$$\text{REFF } (i = 0, e = 30) = \frac{w(\lambda)}{4} \frac{1}{\cos(0) + \cos(30)} \left[\text{P}(g = 30) - 1 + \text{H}(w, \cos(0))\text{H}(w, \cos(30))\right] \tag{64}$$

$$\text{REFF } (i = 60, e = 40) = \frac{w(\lambda)}{4} \frac{1}{\cos(60) + \cos(40)} \left[\text{P}(g = 20) - 1 + \text{H}(w, \cos(60))\text{H}(w, \cos(40))\right] \tag{65}$$

Let us note:

$$\alpha(i = 0, e = 30) = \frac{1}{\cos(0) + \cos(30)} \left[\text{P}(g = 30) - 1 + \text{H}(w, \cos(0))\text{H}(w, \cos(30))\right] \tag{66}$$

$$\alpha(i = 60, e = 40) = \frac{1}{\cos(60) + \cos(40)} \left[\text{P}(g = 20) - 1 + \text{H}(w, \cos(60))\text{H}(w, \cos(40))\right] \tag{67}$$

Then we can define:

$$\text{REFF}(i = 60, e = 40) = ratio \times \text{REFF}(i = 0, e = 30) \tag{68}$$

$$\text{where } ratio = \frac{\alpha(i = 60, e = 40)}{\alpha(i = 0, e = 30)} \tag{69}$$

This ratio allows us to transform a measurement conducted at i = 0 deg and e = 30 deg to an equivalent reflectance spectrum for i = 60 deg and e = 40 deg. However, this method raises a major issue: the variable '*ratio*' on which this method is based depends on the single scattering albedo. The problem is that we do not know the single scattering albedo for each darkened tholin. We can calculate the variable '*ratio*' from the measurements conducted with the pure tholin (which have been performed under various geometries among which we find the two geometries we are interested in). However, we only get one single spectrum under a standard geometry for each of the darkened tholins. If we want to use the method presented above to go from this geometry to the (i=60 deg, e = 40 deg) one, we have to assume that the single scattering albedos of the darkened tholins are somewhat similar to that of the pure tholin (to be able to use the value of *ratio* that we have derived from the pure tholin measurements). There is however no evidence which could support such an assumption, especially as the reflectance levels of the darkened tholins are way lower than that of the pure tholin.

More precisely, when the single scattering albedo w is decreasing, the term $H(w, \cos(i = 0))H(w, \cos(e = 30))$ is more significantly reduced than the term $H(w, \cos(i = 60))H(w, \cos(e = 40))$.

This basically means that the term $\frac{H(w,\cos(i=60))H(w,\cos(e=40))}{H(w,\cos(i=0))H(w,\cos(i=30))}$ is increasing when the single scattering albedo w is decreasing.

If we express the variable *ratio* so that we make this term appear, we obtain the following relation:

$$ratio = \frac{\cos(0) + \cos(30)}{\cos(60) + \cos(40)} \frac{P(g = 20) - 1 + H(w, \cos(60))H(w, \cos(40))}{P(g = 30) - 1 + H(w, \cos(0))H(w, \cos(30))} \tag{70}$$

As a result, we expect the variable *ratio* to increase with the decreasing single scattering albedo w. Consequently, the more darkened the tholins are, the lower their reflectance level and probably their single scattering albedo as well and therefore the higher we can expect the value of the variable *ratio* compared to that determined from the pure tholin measurements.

This is the reason why we expect this corrective method to underestimate the correction to be applied.

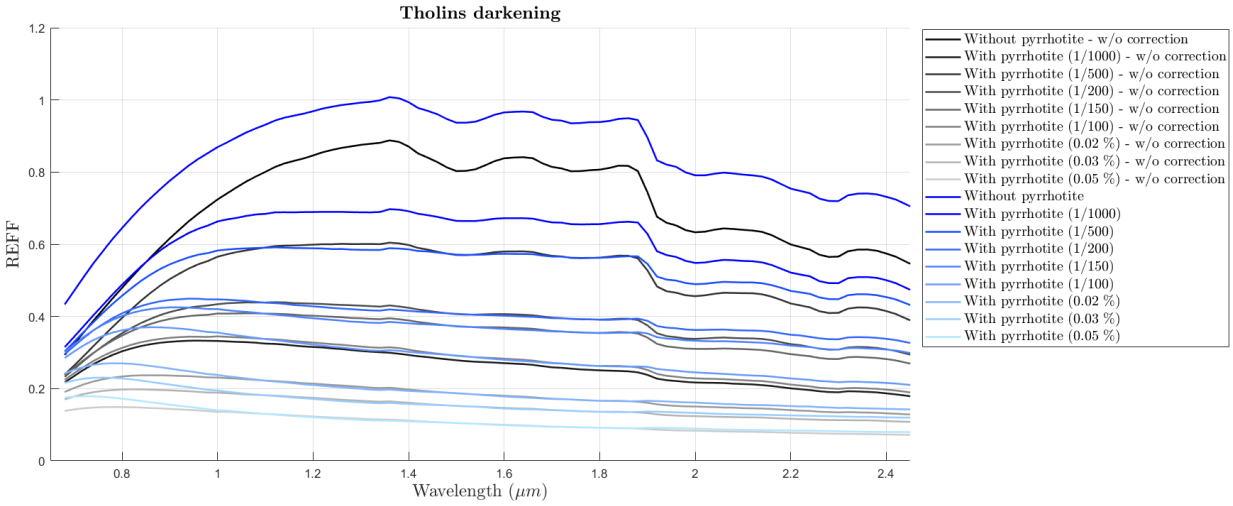

Figure 27: Spectra of darkened tholins, corrected to account for the geometry (first version of the correction)

– Because of this expected underestimation of the correction that we have just applied to take the geometry into account, we are looking for another method.

An alternative solution to get rid of the problem caused by the single scattering albedo differences between pure and darkened tholins would be to inverse Hapke's model for each of the darkened tholins. The main issue of such a technique is that the inversion will be based on one spectrum only. This is a major problem since we cannot guaranteed neither the robustness of such an inversion nor its uniqueness. Nevertheless, processing each darkened spectrum individually appears to be the only method to be totally independent from the value of the single scattering albedo. As we have no indication about how much the single scattering albedo is varying between the different tholins (darkened or not), it seems that the individual inversion of every spectrum could be a nice alternative to a general correction which neglects the single scattering albedo issue.

Applying this second method allows us to compare its results with those obtained with the first method mentioned above. This aims at confirming whether or not the outcomes seem to be logical. Typically, we expect, as previously stated, the results of the first method to be a bit lower than those of the second method.

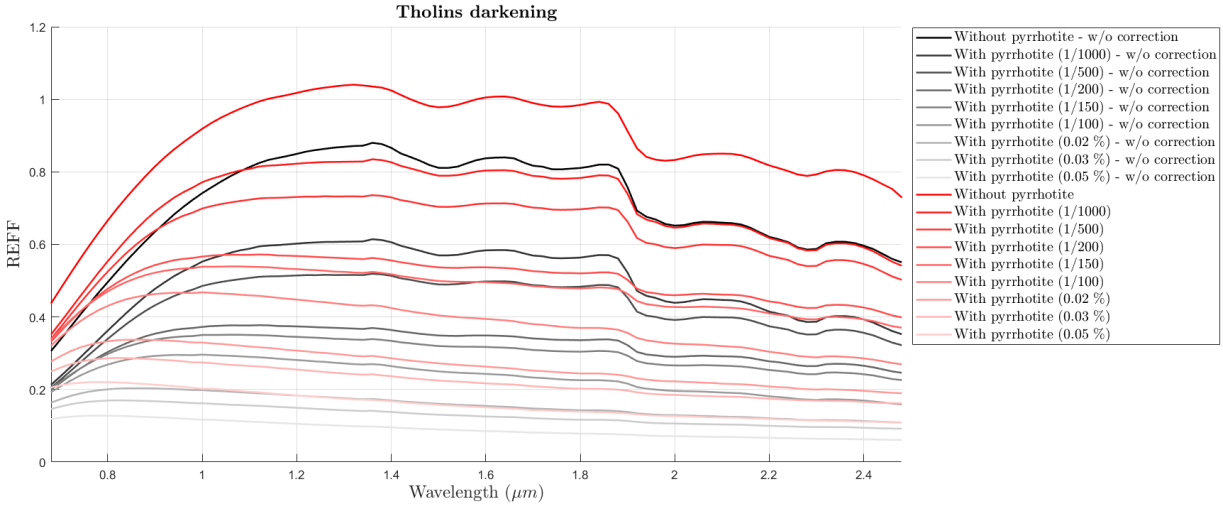

Figure 28: Spectra of darkened tholins, corrected to account for the geometry (second version of the correction)

Consistently with our previous remarks, the second correction increases the reflectance level of darkened tholins more than what the first method does. The darker the tholins are, the higher the difference is between the outcomes of the first and second methods, respectively. This is in agreement with the single scattering albedo issue that has been identified for the first method: indeed, the darker the tholins are, the lower their single scattering albedo is and the more this issue grows significant. In the ideal case (meaning if the two corrective methods were perfectly working), the two methods should have led to the exact same results for the pure tholins (as pure tholins are not concerned with the single scattering albedo issue).

This is a good way to examine the quality of the two methods that have been performed. We see that even if this is not exactly the case, the outcomes of the two methods are relatively similar for the pure tholins (about 4-5 % discrepancies). This confirms the fact that even if neither of the two methods is exact, they both provide consistent results. We should keep in mind that we are not aiming for a very high precision anyway but we rather want to have a good indication of the amount of darkening agent needed to lower the spectral contrast and the decreasing of the reflectance level this will induce. We will keep using the second corrective method in the rest of our work.

8.5 Optimisation of Cthulhu's surface mixture to match New Horizons data

8.5.1 Optimisation principle

The aim of the optimisation algorithm is to model a spatial mixture between CH_4-ice on one side and an intimate mixture of refractories on the other side (composed of C_2H_6-ice, CH_3OH-ice, crystalline H_2O-ice and tholins) and to find the parameters for which the reflectance of this mixture is the closest to that of the New Horizons spectra. Indeed, numerous free parameters have to be determined while modelling such a mixture. First of all, we do not know the mass and spatial fractions of each of the chemical compounds mentioned above (which we suspect to be present on Pluto's surface). We should note that mass fractions in the refractories intimate mixture have to be determined for C_2H_6, CH_3OH, crystalline H_2O and tholins while the spatial ratios of both the refractories and the CH_4 units forming the final surface are unknowns as well. In addition to that, we have to determine the corresponding particle diameters (which are unknowns of our model too). The mass fractions and diameters of each of the components are therefore the optimisation parameters (as it was already the case in **?**, except that we have reduced the number of chemical compounds to be put in our model, compared to what had been done in Cook et al. (2018)).

The optimisation process has been performed with the software Tudat, developed in the Aerospace Faculty of Delft University of Technology and initially dedicated to optimisation problems in astrodynamics. We are not interested in the astrodynamics features of this software here but rather in the Pagmo toolbox which is available in Tudat and which contains the implementation of various optimisation algorithm by ESA. The choice of Tudat whereas this software is not really designed for planetology problems has been motivated by our knowledge of this software and the fact that our previous our previous experiences with this software would make the programming part easier.

The optimisation algorithm is looking for the minimum value of a "fitness" function which characterises how good a solution is (the lowest the fitness value is, the better the solution). In our particular case, the fitness function has been defined as the total sum of squares of the difference between the New Horizons data and the reflectance calculated by our model. The parameters the optimisation process can tune to find this optimum are the mass and spatial fractions and the diameters of the chemical components previously mentioned (CH_4, C_2H_6, CH_3OH, crystalline H_2O and tholins as a reminder).

Some constraints have defined the search space associated with those free parameters: the particles diameters are been constrained between 0.1 μm and 100 μm and the mass fractions are contained between 0 and 1. Additional constraints have been inferred by the inner definition of the mass and spatial fractions: the sum of the refractories mass fractions (forming one of the two spatial units) must be equal to 1 and the sum of the two spatial ratio (one for the CH_4 and the other one for the refractories unit must be equal to 1 as well)).

The Pagmo toolbox offers numerous optimisation algorithms we can select. For this particular project, five different algorithms have been tested. It is beyond the scope of this report to present each of them in details but we will still give a very brief description of their main principle.

- The **Simple Genetic Algorithm (referred as sga in Tudat)** is based on Darwin's natural selection principle. In a given population, each individual represents a solution of our problem. The fitness of this solution defines the "strength" of the individual and therefore its ability to survive. Natural selection is applied from one generation of solutions to the next one, in such a way that the algorithm will progressively converge towards the best individual, meaning the optimum we are looking for.

- The **Differential Algorithm (de)** is a variant of the Genetic Algorithm which represents solutions with bits while differential algorithms deal with real numbers. The difference between these two algorithms concern the way they are implemented but not really the principle they are based on.

- The so-called **de1220** algorithm in Tudat is the self-adaptive version of the differential algorithm.

- The **Predator-Swarm algorithm (pso)** uses the behaviour of a swarm facing with a predator (the swarm globally tends to move as far as possible from the predator) to define how to parse the parameters search space.

- The **Articial Bee Colony algorithm (abc)** is based on the way a bee colony is organised. Each solution corresponds to a food source and the fitness of the solution is represented as the amount of food present in this source. The algorithm will parse the parameters search space and progressively select solutions mimicking the way bees are looking for food.

For each of these algorithms, we need to define the number of generations we want to consider, as well as the number of individuals in each generation. The larger the number of individuals is, the better we parse the parameters search space. The algorithm select individuals in each generation (the way this selection is performed depends on which algorithm we use) to create a new generation with different individuals which are supposed to be better than those of the previous generation. It is therefore extremely important to select a number of generations large enough to allow the optimisation algorithm to converge.

For our particular optimisation problem and after some tuning, we have selected a population of 1000 individuals per generation and 50 generations. This has been a trade-off between the quality of the optimum identified by the algorithm and the computing time required to achieve this optimum. This configuration seems to offer good performances in terms of algorithm convergence. It has also been chosen as a good configuration to start with since it allows the optimisation process to run in about 1 hour only and therefore makes it possible for us to test various tholins (with different darkening ratios for example). The calculations which have led to the best results could be run again refining the optimisation algorithm (meaning either increasing the number

of individuals or generations or even refining the parameters search space after having roughly identified the location of the optimum in the initial search space).

At this point, it is worth stating that the convergence of the algorithm has been tested by running it several times with different initial random seeds. If the algorithm finds the same optimum each time it is re-run, then we can consider the convergence has been reached. This aims at avoiding the identification of local optimum as the global solution to our optimisation problem, which is a major issue in complex problems with many parameters to optimise. However, we should keep in mind that our problem is extremely complex (many free parameters and highly non-linear problem) and that the finding of the exact optimum is not the main goal of our work. The optimisation process is more a technique we wanted to use to derive estimated amount of tholins and ices and because this process is very time-consuming, we have not run calculations until we got the exact same fitness starting from different random seeds. The program would indeed have to be run during several days to achieve such a result and we are not looking for a solution with this degree of precision, mainly because our model is a simplified one and therefore it does not make sense to spend days to achieve a extremely good optimum that we do know to be an approximation anyway. As a result, we have only checked that the fitness values we get with different initial random seed are almost the same and even more important, that the optima found starting with different random seeds are consistent. This means we expect the free parameters values identified by the optimisation process to be very similar when starting from different random seeds.

With 1000 individuals and 50 generations, we have run the five optimisation algorithms presented above for pure tholins with 5% of methane only. Our aim was to determine which algorithm performs better and should therefore be selected. The selection of one single algorithm is required since the number of computations and the time one computation takes do not allow us to perform the entire optimisation process (with different tholins) with several algorithms. The results we obtained are provided in Table 1.

Algorithm	**Fitness value**	**Convergence**
sga	25.282	OK
de	25.635	OK
de1220	25.519	OK
pso	25.294	OK
abc	26.025	NOK

Table 1: Comparison of the performances of different optimisation algorithms

The Simple Genetic Algorithm has performed better than the other ones and it was also one of most advantageous ones regarding the computational time. As a consequence, it has been selected as the algorithm to be used in the rest of our optimisation process.

8.5.2 Optimisation results

The results we have obtained with different tholins on different regions of Pluto's surface and with the two models described in section 3.5 of this report are provided in the tables below. The analysis of these results will not be discussed here. The reader is referred to the section 3.5 for this analysis part.

Tholins	**Fitness value (first random seed)**	**Fitness value (second random seed)**
Pure 95:5 tholins	4.426	4.423
95:5 tholins with pyrrhotite/tholins ratio of 1/1000	5.156	5.147
95:5 tholins with pyrrhotite/tholins ratio of 1/500	6.278	6.280
Pure 99:1 tholins	**2.229**	**2.227**
99:1 tholins with pyrrhotite/tholins ratio of 1/1000	5.156	5.155
99:1 tholins with pyrrhotite/tholins ratio of 1/500	6.303	6.303

Table 2: Optimisation results for the H_2O-poor region of Cthulhu with the first reflectance model (intimate mixtures)

Tholins	**Fitness value (first random seed)**	**Fitness value (second random seed)**
Pure 95:5 tholins	1.084	1.082
95:5 tholins with pyrrhotite/tholins ratio of 1/1000	1.964	1.960
95:5 tholins with pyrrhotite/tholins ratio of 1/500	3.054	3.053
Pure 99:1 tholins	**0.305**	**0.305**
99:1 tholins with pyrrhotite/tholins ratio of 1/1000	1.964	1.967
99:1 tholins with pyrrhotite/tholins ratio of 1/500	3.175	3.170

Table 3: Optimisation results for the H_2O-rich region of Cthulhu with the first reflectance model (intimate mixtures)

Tholins	**Fitness value (first random seed)**	**Fitness value (second random seed)**
Pure 95:5 tholins	3.814	3.811
95:5 tholins with pyrrhotite/tholins ratio of 1/1000	4.415	4.414
95:5 tholins with pyrrhotite/tholins ratio of 1/500	4.574	4.578
Pure 99:1 tholins	**1.896**	**1.899**
99:1 tholins with pyrrhotite/tholins ratio of 1/1000	4.415	4.416
99:1 tholins with pyrrhotite/tholins ratio of 1/500	4.460	4.658

Table 4: Optimisation results for the H_2O-poor region of Cthulhu with the second reflectance model (condensed ices around core tholins)

Tholins	**Fitness value (first random seed)**	**Fitness value (second random seed)**
Pure 95:5 tholins	0.978	0.980
95:5 tholins with pyrrhotite/tholins ratio of 1/1000	1.870	1.873
95:5 tholins with pyrrhotite/tholins ratio of 1/500	2.464	2.459
Pure 99:1 tholins	**0.271**	**0.271**
99:1 tholins with pyrrhotite/tholins ratio of 1/1000	1.870	1.869
99:1 tholins with pyrrhotite/tholins ratio of 1/500	2.462	2.460

Table 5: Optimisation results for the H_2O-rich region of Cthulhu with the second reflectance model (condensed ices around core tholins)

The best parameters our model have estimated for both the two models we used and the two regions of Cthulhu we have considered are provided in the tables below. Between the different initial random seeds we have considered for each calculation, we have selected the parameters estimated by the one which has led to the lowest fitness value. However, differences between parameters estimated with different initial random seeds are very small (as explained before it was something we have checked to ensure our algorithm has globally converged even if the fitness might still evolve a bit from one random seed to another because of the extremely high non-linearity of the problem we are dealing with).

Parameters	**Associated value**
Diameter H_2O crystalline (μm)	$8.5085 \cdot 10^{-1}$
Diameter C_2H_6 (μm)	$3.3900 \cdot 10^{1}$
Diameter CH_3OH (μm)	$8.5609 \cdot 10^{1}$
Diameter tholins (μm)	$8.1560 \cdot 10^{-1}$
Diameter CH_4 (μm)	$8.1654 \cdot 10^{-1}$
Mass ratio H_2O crystalline	$1.8731 \cdot 10^{-1}$
Mass ratio C_2H_6	$1.1031 \cdot 10^{-3}$
Mass ratio CH_3OH	$9.3178 \cdot 10^{-4}$
Mass ratio tholins	$8.1065 \cdot 10^{-1}$
Spatial ratio unit 1	$9.9963 \cdot 10^{-1}$

Table 6: Optimisation results for the H_2O-poor region of Cthulhu with the first reflectance model (intimate mixtures)

Parameters	**Associated value**
Diameter H_2O crystalline (μm)	$7.1580 \cdot 10^{1}$
Diameter C_2H_6 (μm)	$9.0800 \cdot 10^{1}$
Diameter CH_3OH (μm)	$8.7765 \cdot 10^{1}$
Diameter tholins (μm)	1.4358
Diameter CH_4 (μm)	4.8699
Mass ratio H_2O crystalline	$8.8771 \cdot 10^{-1}$
Mass ratio C_2H_6	$2.0739 \cdot 10^{-2}$
Mass ratio CH_3OH	$2.9370 \cdot 10^{-2}$
Mass ratio tholins	$6.2186 \cdot 10^{-2}$
Spatial ratio unit 1	$9.9912 \cdot 10^{-1}$

Table 7: Optimisation results for the H_2O-rich region of Cthulhu with the first reflectance model (intimate mixtures)

Parameters	**Associated value**
Diameter H_2O crystalline (μm)	$8.0278 \cdot 10^{-1}$
Diameter C_2H_6 (μm)	$9.8697 \cdot 10^{1}$
Diameter CH_3OH (μm)	$9.8225 \cdot 10^{1}$
Diameter CH_4 (μm)	$9.0356 \cdot 10^{-1}$
Spatial fraction of tholins into icy grains	$5.9238 \cdot 10^{-1}$
Mass ratio H_2O crystalline	$5.0961 \cdot 10^{-1}$
Mass ratio C_2H_6	$2.9775 \cdot 10^{-1}$
Mass ratio CH_3OH	$1.9264 \cdot 10^{-1}$
Spatial ratio unit 1	$9.6989 \cdot 10^{-1}$

Table 8: Optimisation results for the H_2O-poor region of Cthulhu with the second reflectance model (condensed ices around core tholins)

Parameters	**Associated value**
Diameter H_2O crystalline (μm)	$3.2992 \cdot 10^{1}$
Diameter C_2H_6 (μm)	6.8925
Diameter CH_3OH (μm)	$9.8777 \cdot 10^{1}$
Diameter CH_4 (μm)	$7.9631 \cdot 10^{-1}$
Spatial fraction of tholins into icy grains	$5.2119 \cdot 10^{-2}$
Mass ratio H_2O crystalline	$9.2540 \cdot 10^{-1}$
Mass ratio C_2H_6	$5.8097 \cdot 10^{-2}$
Mass ratio CH_3OH	$1.6498 \cdot 10^{-2}$
Spatial ratio unit 1	$9.6114 \cdot 10^{-1}$

Table 9: Optimisation results for the H_2O-rich region of Cthulhu with the second reflectance model (condensed ices around core tholins)